Materials Today Bio 30 (2025) 101455

Contents lists available at ScienceDirect

Materials Today Bio

journal homepage: www.journals.elsevier.com/materials-today-bio

Doxorubicin-loaded PEGylated liposome modified with ANGPT2-specific peptide for integrative glioma-targeted imaging and therapy

Hongyan Li [a,b,c,d,e,*], Rong Gan [a,e], Jiadi Liu [a,c,d,e], Duling Xu [a,c,d,e], Qiyue Zhang [a,c,f], Haidong Tian [g], Huijun Guo [h], Haijun Wang [i], Zhimin Wang [j], Xianwu Zeng [k]

[a] *Department of Medical Physics, Institute of Modern Physics, Chinese Academy of Sciences, Lanzhou, Gansu, 730000, China*
[b] *Gansu Provincial Isotope Laboratory, Lanzhou, Gansu, 730300, China*
[c] *Key Laboratory of Basic Research on Heavy Ion Radiation Application in Medicine, Lanzhou, Gansu, 730000, China*
[d] *School of Nuclear Science and Technology, University of Chinese Academy of Sciences, Beijing, 101408, China*
[e] *Advanced Energy Science and Technology Guangdong Laboratory, Huizhou, Guangdong, 516029, China*
[f] *School of Nuclear Science and Technology, Lanzhou University, Lanzhou, Gansu, 730000, China*
[g] *School of Life Science and Engineering, Lanzhou University of Technology, Lanzhou, Gansu, 730050, China*
[h] *The First School of Clinical Medicine, Lanzhou University, Lanzhou, Gansu, 730000, China*
[i] *Department of Nuclear Medicine, Gansu Provincial Hospital, Lanzhou, Gansu, 730000, China*
[j] *Department of PET/CT Center, Gansu Provincial Hospital, Lanzhou, Gansu, 730000, China*
[k] *Department of Nuclear Medicine, Gansu Provincial Cancer Hospital, Lanzhou, Gansu, 730050, China*

ARTICLE INFO

Keywords:
ANGPT2
Biomarker
Target peptide
Doxorubicin-loaded nanoliposomes
Glioma-targeted imaging and therapy
Micro-PET/CT

ABSTRACT

Liposomal nanocarriers are able to carry peptides for efficient and selective delivery of radioactive tracer and drugs into the tumors. Angiopoietin 2 (ANGPT2) is an excellent biomarker for precise diagnosis and therapy of glioma. The present study aimed to design ANGPT2-specific peptides to modify the surface of nanoliposomes containing doxorubicin (Dox) for integrative imaging and targeting therapy of glioma. The targeted ANGPT2 peptides were designed using the molecular operating environment. Peptide-conjugated PEGlated liposomes containing Dox (peptide-Lipo@Dox) were prepared for radionuclide and drug delivery. Glioma cell functions were determined based on cell cycle and viability, apoptosis, cell invasion and migration, and colony-formation assays. The anti-tumor effect of peptide-Lipo@Dox was validated in intracranial U87-MG cell glioma-bearing mice *in vivo*. The peptides GSFIHSVPRH (GSF) and HSVPRHEV (HSV) showed specific affinity for ANGPT2 and a better cellular uptake in U87-MG cells. Micro-positron emission tomography (PET)/computed tomography (CT) imaging was used to visualize the orthotopic transplantation of glioma in the brain 1 h after injection of radionuclide ^{68}Ga-labeled peptide-Lipo@Dox. Lipo@Dox with peptide modification demonstrated stable Dox loading, small sizes (<40 nm), and enrichment in the tumor region of the mouse brain. Peptide-Lipo@Dox treatment inhibited the Tie-2/Akt/Foxo-1 pathway, thereby inhibiting cell invasion and migration, cell viability, and colony-forming ability of U87-MG cells. Lipo@Dox peptide modification showed a better suppression of glioma development than Lipo@Dox. Thus, the ANGPT2-specific peptides were successfully designed, and the PEGylated liposome modified with ANGPT2-specific peptide served as part of a potent delivery method for integrative glioma-targeted imaging and therapy.

Abbreviations: Angiopoietin 2, ANGPT2; 1,4,7,10-tetraazacyclododecane-1,4,7,10-tetraacetic acid, DOTA; Phosphate buffered saline, PBS; 4, 6-diamidino-2-phenylindole, DAPI; Real-time quantitative polymerase chain reaction, PCR.

This article is part of a special issue entitled: Biomarker published in Materials Today Bio.

* Corresponding author. Department of Medical Physics, Institute of Modern Physics, Chinese Academy of Sciences, Lanzhou, 730000, China.
E-mail address: lihy@impcas.ac.cn (H. Li).

https://doi.org/10.1016/j.mtbio.2025.101455
Received 16 July 2024; Received in revised form 13 November 2024; Accepted 3 January 2025

1. Introduction

Glioblastoma multiforme (GBM), also known as glioblastoma, is a highly invasive and malignant primary brain tumor [1]. GBM patients generally have a poor prognosis, with the median overall survival (OS) of only 4–6 months and a high incidence of recurrence within 12–15 months [2]. The presence of the blood-brain barrier (BBB) and blood-brain tumor barrier (BBTB) hinders the entry of most chemotherapeutic agents into the brain or the achievement of therapeutic drug concentrations at the tumor site [3], thus greatly impeding treatment effectiveness. Therefore, extensive research efforts have been devoted to developing drug delivery systems that can enhance BBB permeability and target GBM cells.

In recent years, there has been significant interest in lipid-based drug delivery systems that can encapsulate and protect therapeutic drugs, such as doxorubicin (Dox), enhance drug penetration into the brain, and offer advantages, including excellent biocompatibility, low toxicity, and low immunogenicity [4]. Moreover, liposomal radiotracers have been rapidly developing as novel nuclear imaging probes [5]. The liposomal surface can be modified with antibodies, peptides, and carbohydrates to enhance the brain targeting and anti-glioma effects [6]. Previous studies have demonstrated the safety and efficacy of the liposome-Dox drug delivery system in patients with recurrent high-grade glioma [7–9].

Angiogenesis is a necessary process for tumor development. It plays an important role in tumor growth and metabolism and is a promising therapeutic target [10]. The angiopoietin-TEK tyrosine kinase receptor pathway participates in the regulation of vascular permeability and pathological vascular remodeling during tumor angiogenesis and metastasis [11]. Angiopoietin-2 (ANGPT2) binds with tyrosine kinase 2 (Tie-2) to stimulate Tie-2 phosphorylation, thereby promoting cancer cell survival, invasion, and migration [12]. It has been suggested that PI3K/threonine kinase (Akt) is the downstream target of Tie-2 [13]. Moreover, Akt activates Foxo-1, resulting in a significant increase in ANGPT2 mRNA levels and encouraging cell survival in cancer and angiogenesis. Thus, cancer progression is promoted via activation of the PI3K/Akt/Foxo-1 signaling pathway by ANGPT2 [14].

Therefore, we proposed that ANGPT2 activates the PI3K/Akt signaling pathway, phosphorylates Foxo-1, and regulates cell cycle progression, apoptosis, and oxidative stress. It then promotes the proliferation, invasion, and migration of glioma cells. Moreover, ANGPT2 overexpression in GBM based on the cancer genome atlas (TCGA) analysis was verified and shown to be negatively correlated with GBM prognosis. This evidence suggested that ANGPT2 is an excellent glioma biomarker and that ANGPT2 targeting might provide a beneficial diagnostic and therapeutic strategy for GBM.

The present study confirmed for the first time that ANGPT2 regulates the proliferation and apoptosis in glioma cells via the Tie-2/Akt/Foxo-1 pathway. Targeting peptides (GSFIHSVPRH, HSVPRHEV) for ANGPT2 were successfully designed and their high affinity toward U87-MG cell were confirmed. In addition, Dox-loaded nanoliposomes modified with these two peptides were prepared for delivery of radionuclide and antitumor drugs. This method was used for imaging in diagnosis and demonstrated a significant therapeutic effect for intracranial U87-MG cell glioma-bearing mice. Therefore, the study results confirmed ANGPT2 to be an excellent biomarker for precise glioma diagnosis and therapy. They also showed that Dox-loaded nanoliposomes modified with ANGPT2 peptides could be used for imaging and had a targeting therapeutic effect in glioma, providing novel insights into integrative imaging and targeting therapy of glioma.

2. Methods and methods

2.1. Animals and ethics statement

Female BALB/c nude mice of 4–6 weeks age were purchased from Beijing Vital River Laboratory Animal Technology Co., Ltd (Beijing, China) and kept under SPF conditions. The management and handling of animals complied with the administrative regulations of the Laboratory Animal Affairs Administration of the Ministry of Science and Technology of China (1988.11.14). The research on experimental animals was approved by the Ethics Committee of the Institute of Modern Physics, Chinese Academy of Sciences (Approval No: 2021-026), and complied with the Helsinki Declaration.

2.2. Cell culture and transient transfection

T98G (The human malignant glioma cell lines, no. CL-0583) (Procell Life Science&Technology, Wuhan, China) were cultured in MEM medium with 10 % fetal bovine serum (CM-0583, Procell). U251 (The human malignant glioma cell lines, no. CL-0237) (Procell, China), HA (The human astrocyte cell lines, no.1800) (ScienCell Research Laboratories, San Diego, CA, USA), U87-MG (The human malignant glioma cell lines, no. CL-0238) (Procell, China), U87-MG-luc (The human astrocyte tumors cell line, no. WZ0028) (Fenghui Bio, Changsha, China) and bEND.3 (The mouse brain-derived endothelial cells.3, no. TCM-C715) (Hycyte Biotechnology, Suzhou, China) were cultured in DMEM medium with 10 % fetal bovine serum. HUVECs (Human umbilical vein endothelial cells) (Tongpai biotechnology, Shanghai, China) were cultured in endothelial cell medium (no. 1001, Sciencell, USA). All cells were kept under 37 °C with 5 % CO_2.

2.3. Plasmids, antibodies, and siRNAs

Lipo2000 (no. 11668019, Invitrogen, CA, USA) was used for transient transfection. β-actin (no. ab8227), Tie-2 (no. 19157-1-AP), ANGPT1 (no. 27093-1-AP), ANGPT2 (no. no. 24613-1-AP) and Foxo-1 (no. 18592-1-AP) (Proteintech, Wuhan, China), phospho-Tie-2 (Tyr992) (no. Bs-3449R) (Bioss biotechnology, Beijing, China), Akt (no. 4691), phospho-Akt (Ser473) (no. 4060) and Cleaved Caspase-3 (no. 9661L) (Cell Signaling Technology, Bosto, MA, China), phospho-Foxo-1A (Ser256) (no. ab131339) and Caspase-3 (no. ab184787) (Abcam, Cambridge, UK), Bax (no. GTX109683) and Bcl-2 (no. GTX100064) (Genetex, NJ, USA), Ki-67 (no. GB111141) (Servicebio biotechnology, Wuhan, China) were used for analysis of immunoblotting, immunofluorescence and immunohistochemistry. Three different sequences of siRNA of each gene was synthesized by Genepharma (Shanghai, China); their sequences were shown in Supplementary File 1.

2.4. Liposomes

Dox, N-hydroxysulfosuccin-imide (S-NHS), 1,2-distearoyl-sn-glycero-3-phosphoethanolamine (DSPE), 1,2-distearoyl-snglycero-3-phosphoethanolamine-N-[meth-oxy(polyethyleneglycol)-2000] (DSPE-PEG2000), and 2-distearoyl-sn-glycero-3-phosphoethamolamine-N-[carboxy(polyethyleneglycol)2000] (DSPE-PEG2000-COOH), soybean phosphatidylcholine (SPC) were obtained from Avanti Polar Lipids (Alabaster, AL, USA). DSPE-PEG2000- 1,4,7,10-tetraazacyclododecane-1,4,7,10-tetraacetic acid (DOTA) (R-0225), DSPE-PEG2000-Cyanine 5.5 (Cy5.5) (R-PEG-6111) (Ruixi biological technology, Xi'an, China). N,N-Dimethylformamide (DMF) (01155059) was received from Titan Science and Technology Co., Ltd. (Shanghai, China).

2.5. Peptide design and molecular docking

The structure-based drug design module in the Molecular Operating Environment (MOE) (Chemical Computing Group, Montreal, Quebec, Canada) software was used to design peptides. By analyzing the binding patterns of peptides and receptors and selecting suitable side chain hydrogen atoms as connection points according to the structure distribution of peptides in binding pockets, peptide fragment growth was performed by searching the three-dimensional (3D) conformation fragment library in the MOE. Docking was performed to obtain a population of possible conformations and orientations for the ligand at the binding site. Each new generated peptide was given a synthetic feasibility score on a scale of 0–1, with 1 indicating that it is completely synthesizable and 0 indicating that it is not. All candidate peptides were optimized based on energy minimization, and affinity scoring function was used to evaluate the binding free energy of the modified candidate peptides and receptor. Based on the receptor structure (human ANGPT2; PDB ID: 2GY7), the binding site was set around the residues I434, D448, C450, P452, N467, Y475, and S480. All ligand bonds were set to be rotatable. All calculations for protein-fixed ligand-flexible docking were performed using the Lamarckian Genetic algorithm method. The best conformation with the lowest binding energy was chosen after the docking search was completed. The atomic distance for binding sites between peptides and receptor was <4.5 Å.

HDOCK sever was used for molecular docking of peptides with human ANGPT2 protein. The MOE Protein Builder was used to build the 3D structures of targeting peptides GSFIHSVPRH (GSF) and HSVPRHEV (HSV). The 3D ANGPT2 crystal structure (PDB ID: 2GY7) was downloaded from the protein structure database (http://www.rcsb.org). The ANGPT2 was set as the receptor and the peptides were set as ligands. The HDOCK server automatically predicted their interaction through a hybrid algorithm of template-based and template-free docking. The server carried out template-based modeling of the receptor and ligand molecules by searching the PDB for putative homologous templates based on the protein sequences. The intermolecular contacts from the most probable configurations were further analyzed in the MOE. Ten representative peptide conformations were selected after conformer clustering. The interactions between complexes were mapped using PyMol (http://www.pymol.org) [15].

2.6. *Affinity analysis*

The binding of ANGPT2 proteins and peptides was determined using bio-layer interferometry technology based on the Octet system (RE96E, Fortebio, USA). The HPLC and MS results for GSF and HSV identification are shown in Fig. S1 and Fig. S2, respectively. First, 20 μg/mL of ANG PT2 protein in phosphate-buffered saline (PBS, pH 7.4) was immobilized on the surface of an NTA chip. Then, 100 μM peptide (in PBST, pH 7.4) was added dropwise to the NTA chip. Data processing and analysis were performed using ForteBio data analysis software version 10.0 [16].

2.7. *BBB and BBTB penetration analysis*

The HPLC and MS results for FITC-GSF and FITC-HSV identification are shown in Fig.S3 and Fig.S4, respectively. bEND.3 cells or HUVECs were seeded in the upper chamber and five times the number of U87-MG cells were seeded in the lower chamber of the Transwell and co-cultured for 72 h to simulate the BBB and BBTB *in vitro* [17,18]. Then, endothelial cell culture medium was replaced with DMEM containing 10 % fetal bovine serum and FITC-GSF/HSV at a final concentration of 20 μg/mL was added to the upper chamber. The upper- and lower-chamber cells were collected for flow measurement based on cell fluorescence intensity after 4 h and 8 h. The lower-chamber cells were stained with 5 μg/mL of 4′,6-diamidino-2-phenylindole (DAPI) for 10 min, covered with coverslips, and observed under a confocal laser microscope (LSM, Carl Zeiss AG, Germany).

2.8. *Liposome preparation and characterization*

The structure and synthesis routes of DSPE-PEG2000-GSF/HSV are shown in Fig. S5. First, 100 mg of DSPE-PEG2000-NHS was dissolved in 3 mL of DMF. Then, GSF/HSV and triethylamine (molar ratio: 1.1:3) were added and reacted at room temperature for 12 h. The reaction solution was transferred to a dialysis bag (with a molecular weight of 1500 Da) and dialysis was performed in pure water for 24 h. The final product was collected after freezing and drying and confirmed using H nuclear magnetic resonance spectroscopy (Fig. S6). Liposome loading with Dox modified with peptide was performed as follows: 1.5 mg of DSPE-PEG2000 (or modified peptide), 1.5 mg of DSPE-PEG2000-DOTA, 0.4 mg of DSPE-PEG2000-Cy5.5, and 20 mg of SPC were dissolved in 3 mL of chloroform, rotary-evaporated at 40 °C to form a film, and hydrated by adding 250 mM $(NH4)_2SO_4$ solution. After ultrasonic dispersion, the liposome solution with a suitable particle size was prepared using a liposome extruder (Ruixi), placed in a nanodialysis device (Ruixi), and dialyzed in 50 mM PBS (pH 7.4) overnight to remove uncoated $(NH4)_2SO_4$. The liposome solution was then removed. Then, 2 mg of Dox (Ruixi) was added and incubated at 50 °C for 1 h. Next, dialysis was carried out for 1 h to remove unloaded Dox. The absorption was measured in order to determine Dox concentration based on the standard Dox absorption. Then, lipid dispersion was performed through a series of polycarbonate membranes with a pore size ranging from 200 nm to 50 nm using an Avanti Mini Extruder (Avanti Polar Lipids, AL, USA). Dox-loaded liposomes were prepared using a traditional ammonium sulfate gradient loading method according to previously reported procedure [19].

The particle size and zeta potential of the liposomal carriers were characterized using photon correlation spectroscopy (Malvern Instruments Ltd., Worchestershire, UK) and nanoparticle potential analysis (ZET-3000HS, Malvern Instruments Ltd., Worchestershire, UK), respectively. The morphological examination of liposomes was performed via transmission electron microscopy (TEM, JEM1200, Japan) using negative staining with 2 % phosphotungstic acid solution. Encapsulation efficiency was determined using a previously reported method [20]. Briefly, 1 mL of liposome dispersion solution was eluted with PBS (pH 7.4) through a Sephadex G-100 column to remove unloaded Dox.

2.9. *The targeting of peptides for glioma in vivo*

The HPLC and MS results for DOTA-GSF and DOTA-HSV identification are shown in Fig.S7 and Fig.S8, respectively. ^{68}Ga was eluted from a^{68}Ge/^{68}Ga generator system (Eckert and Ziegler, Germany) with 0.1 M HCl. Then, 10 μg of DOTA-GSF/HSV was mixed with 200 μL of NaAc and 1 mCi ^{68}Ga solution (200 μL in 0.1 M HCl) and incubated at 90 °C for 15 min. Next, 300 μg of DOTA-GSF/HSV-Lipo@Dox was mixed with 200 μL of NaAc and 1 mCi ^{68}Ga solution (200 μL in 0.1 M HCl) and incubated at 50 °C for 20 min. Orthotopic U87-MG cell glioma-bearing mice were injected with 100 μCi of ^{68}Ga-DOTA-GSF/HSV or ^{68}Ga-DOTA-GSF/HSV-Lipo@Dox via tail vein and underwent a static animal PET/CT scan for imaging of brain at 30 min after injection, and imaging was reconstructed using the PMOD software (PMOD Technologies, Unitectra zurich, Switzerland). The radioactive uptake was calculated as a percentage of the injected dose per gram tissue (%ID/g) through measuring gamma counts of brain 1 h after injection (150 μCi of ^{68}Ga-DOTA-GSF/HSV or 50 μCi of ^{68}Ga-DOTA-GSF/HSV-Lipo@Dox per mouse).

2.10. *Immunoblotting*

Total protein samples in the supernatant were collected. After quantification using a BCA kit, the protein was separated using 10 % SDS-PAGE gels and then transferred to PVDF membranes (Millipore, Bedford, MA, USA). The membranes were blocked with 5 % nonfat milk powder in TBST followed by the addition of primary antibody and incubation at 4 °C overnight. The membranes were then washed with TBST after incubation with secondary antibody and the protein bands were detected using a chemiluminescence reagent kit (New Cell & Molecular Biotech, Suzhou, China) [21].

2.11. *Immunofluorescence and immunohistochemistry*

Immunofluorescence assay was performed according to the procedure described in a previous study [22]. Briefly, after permeabilization, blocking with 5 % BSA in TBS, incubation with a primary antibody (1:100) overnight at 4 °C, and staining with 5 μg/mL of DAPI, the cell slides were covered with coverslips and observed under a biomicroscope (BX53, Olympus, Tokyo, Japan) or scanned under a confocal laser microscope (LSM, Carl Zeiss AG, Germany).

Brain and xenograft tumor samples were analyzed using immunohistochemistry as previously described [23]. Tissue microarray results were obtained from 180 patients at Shanghai Zhuoli Biotechnology Company Ltd. The TMA samples were scanned with a NanoZoomer S210 (Hamamatsu, Japan) and xenograft tumor sections were analyzed using Panoramic MIDI software (3DHISTECH, Budapest, Hungary).

2.12. *Cell cycle and apoptosis analysis*

The cells were collected for apoptosis and cycle analyses. After fixing with 70 % ethanol, the cells were resuspended in cool PBS. Next, 50 μg/mL of propidium iodide (PI) (Meilune) was added to the suspension and incubated at 37 °C for 30 min in the dark. Then, the DNA contents were analyzed using the ModFit software (Verity Software House, New York, USA). The apoptosis ratios were determined using Annexin V/PI kit (Meilune biological technology, Dlian, China).

2.13. *Reverse transcription and quantitative polymerase chain reaction analyses*

The DDCt method was used to analyze the expression levels of target genes in different groups. The primers used were 5′- ACACCACGAATGGCATCTA-3′ and 5′-GGGTTACCAAATCCCACTTTAT-3 ′ (ANGPT2); 5′-TCAAGAAGGTGGTGAAGCAGG-3′ and 5′-TCAAAGGTGGAGGAGTGGGT -3′ (GAPDH) [24].

2.14. *Cell viability assay*

Cell viability was detected using a cell counting kit-8 (CCK-8) (Meilune). Cells were treated with equivalent concentrations of Dox in Lipo@Dox formulations for 24 h. Then, 10 μL of the CCK-8 reaction solution was added to each well and incubated at 37 °C for 4 h. The 96-well plates were placed in a microplate reader (Infinite M200, Tecan, Switzerland) to measure the absorbance at a wavelength of 450 nm. The following formula for cell viability was used to calculate the growth percentage: (%) = [A (compound +)–A (blank)]/[A (compound–)–A (blank)] × 100 % [25].

2.15. *Colony formation assay*

U87-MG cells were seeded into 35-mm culture dishes. Upon reaching 70 % confluence, siRNA-ANGPT2 and pEX-3-ANGPT2 plasmids were added to the wells for 48-h transfection. In addition, 1 μg/mL of Dox (equivalent concentration of Dox) and Lipo@Dox formulations were added and incubated for 24 h. The cells were then digested with 0.25 % trypsin and washed three times with PBS. Next, 1300 cells were seeded into 35-mm culture dishes or six-well plates and cultured at 37 °C with 5 % CO_2 for 14 days. The cells were then washed three times with PBS, fixed with methanol, and stained with 0.2 % crystal violet. Each group was assayed in triplicate. The number of colonies was observed and counted [26].

2.16. *Transwell cell invasion and migration assay*

U87-MG cells were transfected with siRNA-ANPT or pEX-3-ANPT plasmids for 48 h and treated with 1 μg/mL of Dox (equivalent concentration of Dox) and Lipo@Dox formulations for 24 h. Transwell chambers (Corning Costar) were used for Transwell invasion assays as previously described [27]. Specifically, 100 μL of Matrigel with a final concentration of 1 mg/mL was added to the center of the bottom of the upper Transwell chamber and incubated at 37 °C for 4–5 h to dry. Then, 200 μL of the cell suspension for each group was placed in the upper Transwell chamber and cultured in a 37 °C and 5 % CO_2 incubator for 24 h.

2.17. *In vivo imaging and anti-tumor verfication*

U87-MG cell suspension (1 × 10^5 cells/mL) was injected into the right brain (striatum, 1.8 mm right lateral to the bregma and 3 mm deep) of nude mice to establish intracranial orthotopic glioma model [28]. Micro-magnetic resonance imaging (MRI) (Xingaoyi Medical Equipment Co., Ltd., OPER-1.0, Ningbo, China) was performed to check whether the model was established successfully. The mice were administered 5 mg/kg of Dox via tail vein seven days post-implantation. Brain tumor fluorescence and drug distribution were visualized using a whole-body *in vivo* fluorescence imaging system (Perkinelmer Co., Ltd., IVIS Lumina LT Series III, Waltham, MA, USA). Drug distribution was monitored 0, 2, 6, 24, and 30 h after administration. The fluorescence imaging of organs was performed 30 h after drug administration. Since 2.5 mg/kg of Dox is often used to verify the *in vivo* anti-tumor effect of Dox-loaded nanoparticles [29,30], the drug was injected every three days while the tumor volume was monitored via bioluminescence imaging (BLI) using an *in vivo* fluorescence imaging system and MRI. The body weight was measured at the same time. After 15 days of treatment, the heart, liver, spleen, lung, and kidney were excised and separated for paraffin tissue sections. Apoptotic cell death in glioma tissues was detected using a TdT-mediated dUTP nick end labeling kit (TUNEL) (Servicebio). Then, glioma sections were stained with hematoxylin and eosin (H&E) to evaluate tumor cell apoptosis.

2.18. *Biochemical tests for renal function*

Whole blood samples were collected after treatment from the orbit of mice and measured using a blood biochemistry analyzer to detect creatinine (CREA), blood urea nitrogen (BUN), and uric acid (UA) levels.

2.19. *Statistical analysis*

GraphPad prism 8.0 software (GraphPad Software, CA, USA) was used to analyze the data. Student’s t-test and one-way analysis were used to analyze the statistical differences.

3. Results

3.1. *ANGPT2 is an excellent biomarker of glioma*

ANGPT2 expression was higher in GBM and second only to renal clear cell carcinoma compared to the levels in other malignant tumors (Fig. 1A). ANGPT2 mRNA showed significantly high expression in GBM than in normal tissues (Fig. 1B). Moreover, higher grade of brain tumor with higher ANGPT2 mRNA expression was noted (Fig. 1C), although there were no significant differences in gender (Fig. 1D). Higher ANGPT2 mRNA expression was also observed in GBM patients older than 42 years (Fig. 1D). In addition, high mRNA ANGPT2 expression was associated with poorer OS (Fig. 1E) and disease-free survival (Fig. 1F). These results indicate that ANGPT2 expression levels were significantly negatively correlated with prognosis in GBM patients. A total of 180 brain tumor specimens with stages I–IV were provided by Zhuoli Biotechnology (Shanghai, China) to determine the ANGPT2 expression using a tissue microarray. Representative images of immunohistological ANGPT2 staining are shown in Fig. 1G. Since ANGPT2 is a secreted protein, it is localized in the cytoplasm, membrane, and intercellular substance (Fig. 1H). The ANGPT2-positive areas were increased in a high-grade brain tumor (Fig. 1I). The above results indicate that ANGPT2 was highly expressed in GBM. Therefore, ANGPT2 can be an excellent target for GBM treatment. The ANGPT2 expression in astrocytes and glioma cells was compared to determine the ANGPT2 levels in

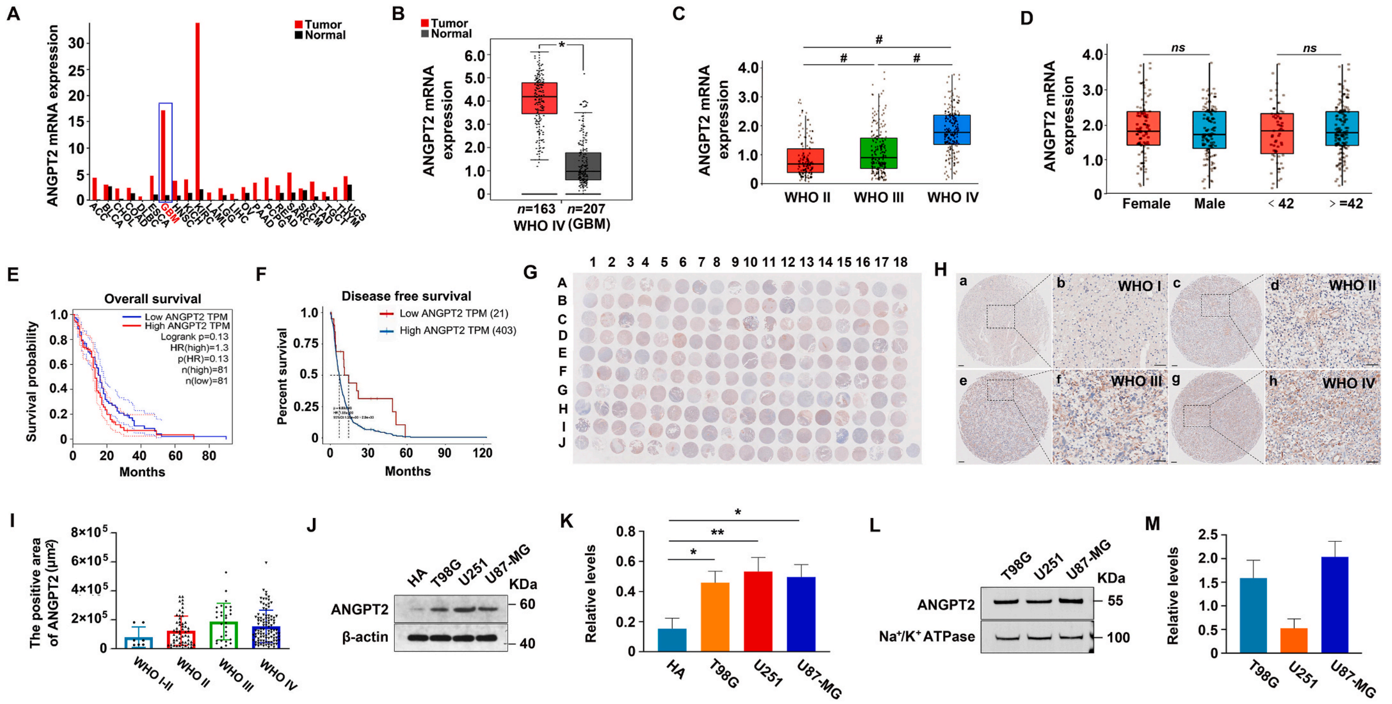

Fig. 1. High ANGPT2 expression correlates with GBM progression and poorer prognosis. (A) ANGPT2 mRNA expression in different malignant tumors (http://gepia.cancer-pku.cn/). (B) Comparison of ANGPT2 mRNA expression between normal brain and GBM tissues from TCGA datasets. (C) ANGPT2 mRNA expression in brain tumor at different stages (http://www.cgga.org.cn/), $^{\#}p < 0.001$. (D) ANGPT2 mRNA expression in brain tumor at WHO stage IV in individuals of different gender and age (http://www.cgga.org.cn/). (E) Kaplan-Meier curves estimating overall survival and (F) disease-free survival (https://smuonco.shinyapps.io/PanCanSurvPlot) in patients of ANGPT2 mRNA in GBM. Log-rank test, $p < 0.001$. (G) The observation of ANGPT2 protein expression in different stages of brain tumor tissues. (H) Representative images of ANGPT2 protein expression (a, c, e, and g, magnification 5 × ; b, d, f, and h, magnification 200 × , bar = 50 μm). (I) Positive rate of ANGPT2 in glioma in different stages of brain tumor tissues. (J, K) ANGPT2 expression was analyzed using IB in HA, T98G, U251, and U87-MG cells. ANGPT2 expression was quantified (ANGPT2/β-actin). Normalized ANGPT2 in HA cells was set at 1.0. $^{*}p < 0.05$, $^{**}p < 0.01$ ($n = 3$). (L, M) ANGPT2 levels in membrane proteins were analyzed using IB in T98G, U251, and U87-MG cells. The level of ANGPT2 was quantified (ANGPT2/Na^{+}-K^{+} ATPase). IB, immunoblotting; HA, human astrocyte cell.

GBM cells. The results showed that the expression of ANGPT2 in T98G, U251, and U87-MG cells was higher than that in human astrocytes (Fig. 1J and K). Membrane receptor proteins account for ~70 % of United States Food and Drug Administration-approved drug targets [31]. Although ANGPT2 is a secreted protein, it binds with Tie-2 to regulate physiological processes. Thus, the high level of ANGPT2 on the membrane is a prerequisite for achieving targeted ANGPT2-based therapy. The ANGPT2 level was highest in the membrane proteins of U87-MG cells than in those of T98G and U251 cells (Fig. 1L and M). Moreover, morphological observation showed that ANGPT2 was more expressed on U87-MG cell protrusions (Fig. 2A). Therefore, U87-MG cells were selected for follow-up experiments.

The knockdown efficiency of ANGPT2 mRNA for different siRNAs is shown in Supplementary File 2. The fluorescence ANGPT2 signal was weakened after ANGPT2 silencing and enhanced after overexpression in U87-MG cells (Fig. 2B). ANGPT2 silencing increased the apoptotic ratio (Fig. 2C), promoted G1 phase arrest (Fig. 2D), and inhibited cell viability (Fig. 2E). However, ANGPT2 overexpression decreased the apoptotic ratio (Fig. 2C) and increased the S-phase ratio (Fig. 2D) and cell viability (Fig. 2E). Representative flow cytometry images are shown in Fig. S9. In addition, ANGPT2 silencing inhibited colony formation (Fig. 2F and G), invasion (Fig. 2H and I), and migration (Fig. 2J and K) of U87-MG cells, while ANGPT2 overexpression did the opposite.

3.2. ANGPT2 actives the Tie-2/Akt/Foxo-1 pathway to promote glioma cell proliferation

Co-IP technology was used to detect the binding of Tie-2 with ANGPT1 and ANGPT2. Western blotting analysis showed that the interaction between Tie-2 and ANGPT1 and ANGPT2 was weakened after ANGPT2 knockdown (Fig. 2L; lane 3 compared to lane 2 in the upper panel) and enhanced after overexpression (Fig. 2L; lane 6 compared to lane 5 in the upper panel). Moreover, the phosphorylation levels of Tie-2, Akt, and Foxo-1 decreased after ANGPT2 knockdown (Fig. 2M and N). However, ANGPT2 overexpression increased their phosphorylation levels (Fig. 2M and N). In addition, the expression of cleaved-caspase 3 and Bax increased, while the expression of Bcl-2 decreased after ANGPT2 knockdown (Fig. 2O and P). Therefore, ANGPT2 silencing likely weakened the interaction of Tie-2 with ANGPT1 and ANGPT2 and then inhibited the Tie-2/Akt/Foxo-1 pathway to hinder proliferation and promote U87-MG cell apoptosis.

3.3. ANGPT2 peptide ligand design and affinity of target peptide with ANGPT2

Based on the X-ray crystal structure of ANGPT2 obtained from the protein data bank, MOE was used to design the specific peptide ligand for ANGPT2. Considering the influence of peptide length and molecular weight on BBB crossing, the length of the targeted peptide should be minimized while ensuring its stability and activity. Therefore, the length of the octapeptide or decapeptide was used as the binding window. The binding conformations of peptides and receptors were generated using a custom MacroModel sampling method. Ten representative conformations were selected after clustering.

The affinity assay results showed that the GSF and HSV had a strong affinity for ANGPT2 protein with respective KD values of 3.43 μM and 50.2 nM. The affinity results represent rapid binding and dissociation of peptides with the ANGPT2 protein (Fig. 3A and B). The binding modes

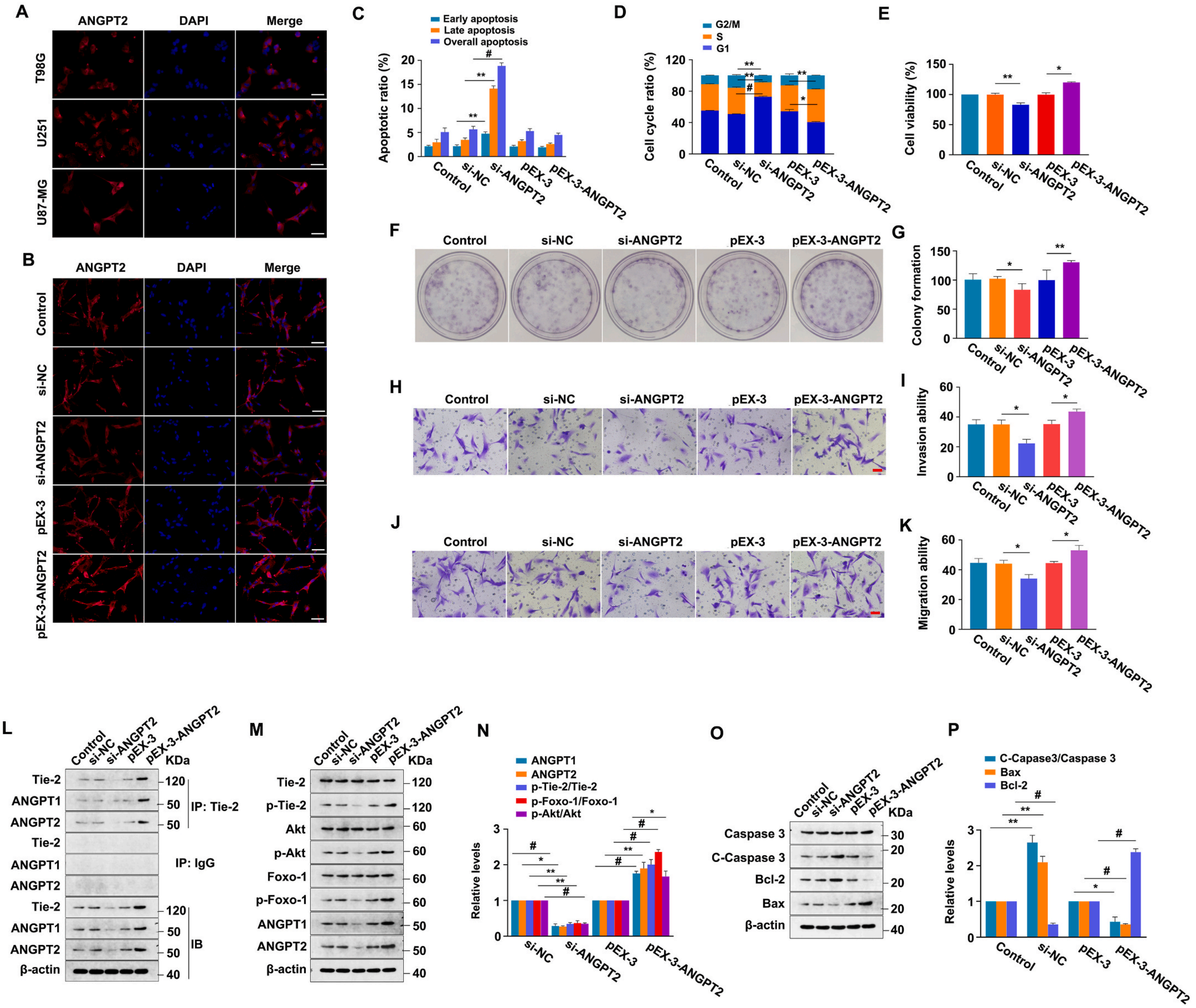

Fig. 2. ANGPT2 promoted apoptosis and inhibited viability and Tie-2/Akt/Foxo-1 pathway in U87-MG cells. (A, B) IF staining with ANGPT2 antibody in different glioma cells and transfected U87-MG cells; DAPI staining shows nucleoli (magnification, 400 × , bar = 50 μm). (C–G) U87-MG cells were transfected with ANGPT2-siRNA or overexpressed plasmid pEX-3-ANGPT2 for 48 h. (C) Apoptosis percentage was analyzed using flow cytometry; $**p < 0.01$, $^{\#}p < 0.001$ ($n = 3$). (D) Cell cycle was analyzed using flow cytometry; $*p < 0.05$, $**p < 0.01$, $^{\#}p < 0.001$ ($n = 3$). (E) Cell viability was measured using CCK-8 assay; $*p < 0.05$, $**p < 0.01$ ($n = 3$). (F) Colony formation was observed and (G) calculated; $*p < 0.05$, $**p < 0.01$ ($n = 3$). (H–K) NC and transfected U87-MG cells were seeded into transwell chambers. (H) Cell invasion in the lower chamber was observed (magnification, 200 × , bar = 50 μm) and (I) the number of cells was counted; $*p < 0.05$ ($n = 3$). (J) Cell migration in the lower chamber was observed (magnification, 200 × , bar = 50 μm) and (K) the number of cells was counted; $*p < 0.05$ ($n = 3$). (L–P) U87-MG cells were transfected with ANGPT2-siRNA or pEX-3-ANGPT2 for 48 h. (L) Analysis of ANGPT2 interaction with Tie-2 for co-IP assays with Tie-2 antibody. (M, O) Protein levels were detected using IB. Protein expression was quantified (target protein/β-actin) and normalized target protein in NC or vector cells was set to 1.0 (N, P); $*p < 0.05$, $**p < 0.01$, $^{\#}p < 0.001$ ($n = 3$). IB, immunoblotting; IP, immunoprecipitation; co-IP, co-immunoprecipitation; IF, immunofluorescence.

between peptides and ANGPT2 are shown in Fig. 3C and D. In the binding mode between GSF and ANGPT2, the Asp448 residue in ANGPT2 forms a salt bridge with the Arg9 residue in GSF. The Cys450, Gly451, and Tyr476 residues in ANGPT2 form a hydrogen bond with the Arg9 and His 10 residues in GSF. In the binding mode between HSV and ANGPT2, the Cys433, Cys450, and Tyr476 residues in ANGPT2 form a hydrogen bond with the Arg5 and His1 residues in HSV. The Tyr475 residue in ANGPT2 forms a hydrophobic interaction with the His1 residue in HSV. The FITC-GSF/HSV and DOTA-GSF/HSV syntheses are shown in Fig. 3E–J.

3.4. Peptide uptake in U87-MG cells

The effects of peptides administered at different concentrations on the viability of U87-MG cells, bEND.3 cells, or HUVECs were measured using the CCK-8 assays (Fig. 4A and B). The peptides showed stronger inhibition of U87-MG cells than bEND.3 cells and HUVECs. The bEND.3 cell viability showed no changes even after addition of 100 μg/mL of GSF. However, the viability of U87-MG cells was decreased in a dose-dependent manner, indicating that the target peptides had low cytotoxicity in brain microvascular endothelial cells. Then, bEND.3 cells or HUVECs and U87-MG cells were co-cultivated in the Transwells to simulate the BBB and BBTB (Fig. 4C). Flow cytometry (Fig. 4D) and immunofluorescence (Fig. 4E) results showed that the fluorescence

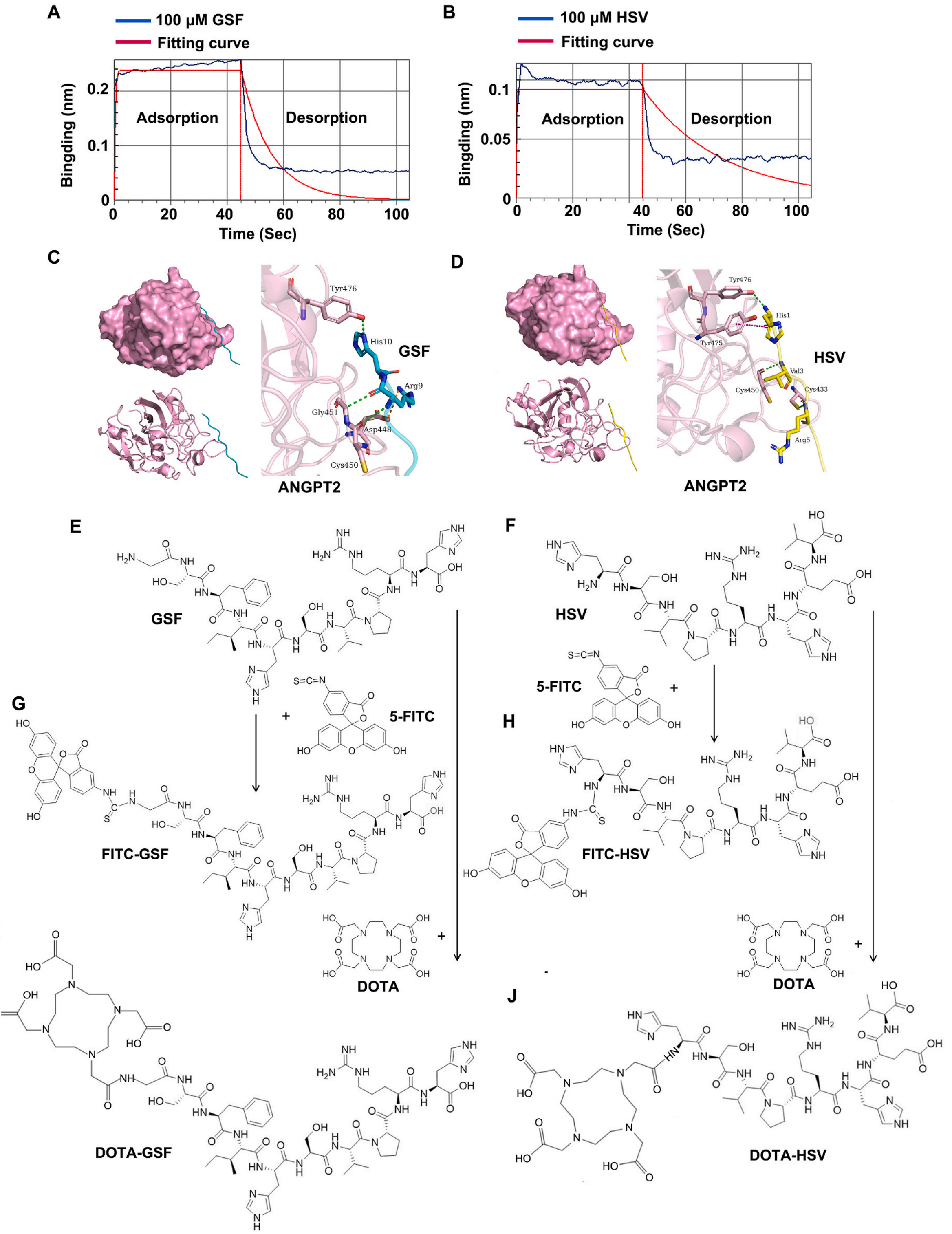

Fig. 3. Affinity analysis and reaction scheme for targeting probe. (A, B) Affinity analysis of ANGPT2 and GSF/HSV. Red line represents the fitting curve using multiple automatic fits, while blue and green lines represent the test curve. (C, D) Docked positions of GSF and HSV with ANGPT2 shown as a cartoon model in yellow and blue. (E–J) Reaction scheme for GSF and HSV with FITC and DOTA. (For interpretation of the references to color in this figure legend, the reader is referred to the Web version of this article.)

intensity of FITC in U87-MG cells increased over time, indicating that the peptides penetrated the vascular endothelial cells and were taken up by glioma cells. Moreover, GSF fluorescence intensity was stronger than that of HSV (Fig. 4F and G), showing that GSF had a better targeting effect.

To investigate the ability of HSV/GSF to enter the brain and target gliomas, DOTA labeled with radionuclide ^{68}Ga was used to modify the two peptides. Micro-PET/CT imaging (Fig. 4H) was used to visualize the orthotopic tumor transplantation of U87-MG cells in the brain 30 min after injection of ^{68}Ga-DOTA-GSF/HSV and compared to the ^{68}Ga-DOTA. Brain gamma counts in the ^{68}Ga-DOTA-GSF/HSV group were greater than those in the ^{68}Ga-DOTA group (Fig. 4I and J). This further

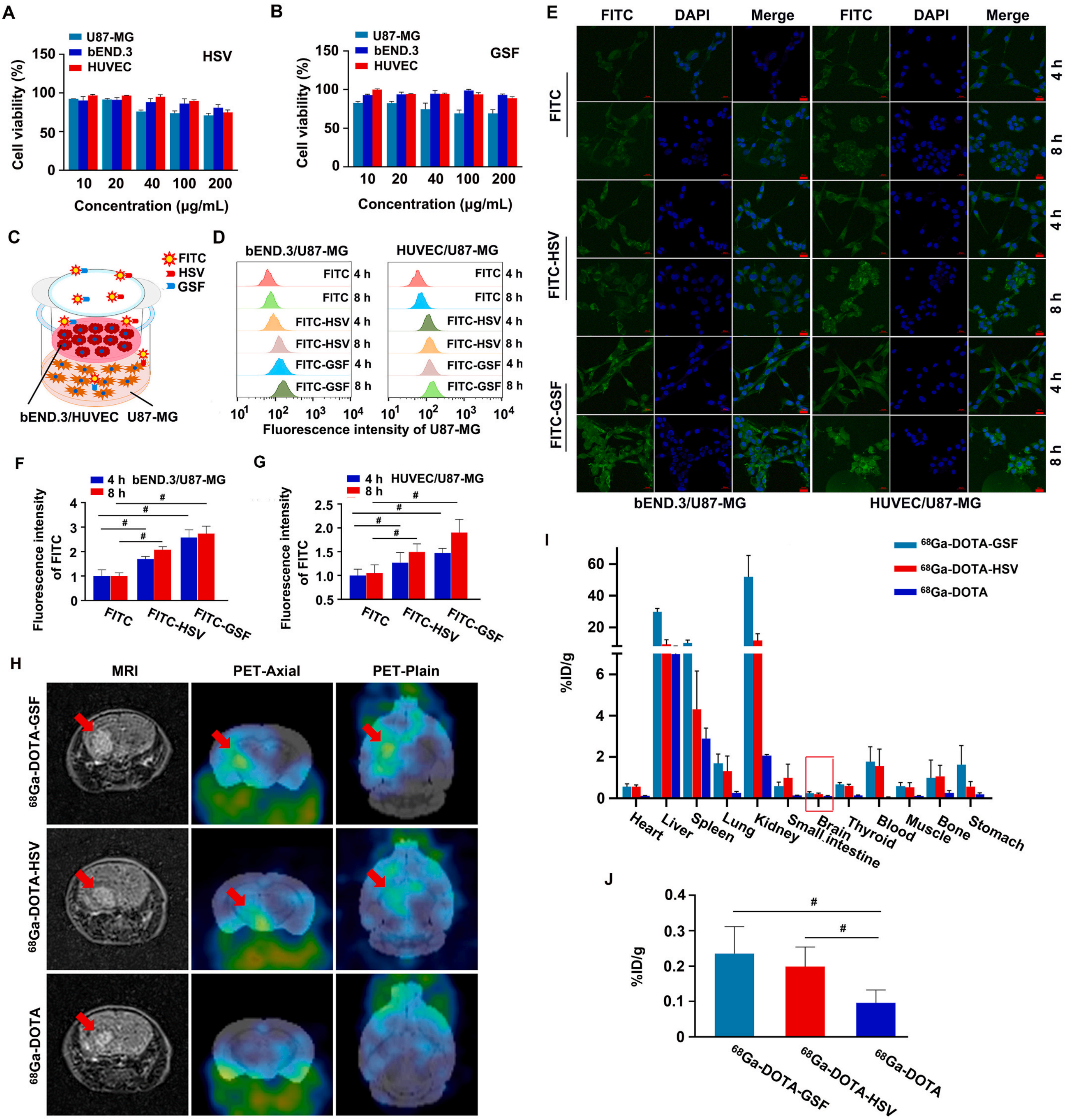

Fig. 4. Targeting peptide uptake in U87-MG cells. (A, B) GSF and HSV effects on U87-MG cells, bEND.3 cells, and HUVECs. (C) Uptake process of FITC-labeled GSF and HSV in U87-MG cells co-cultivated with bEND.3 cells and HUVECs. (D) Flow cytometry analysis of FITC-labeled GSF and HSV uptake in U87-MG cells. (E) Immunofluorescence analysis of FITC-labeled GSF and HSV uptake in U87-MG cells; DAPI staining shows nucleoli (magnification, 400 × , bar = 50 μm). (F, G) Fluorescence intensity of FITC-labeled GSF and HSV in U87-MG cells. $^{\#}p < 0.001$ was calculated using ANOVA ($n = 6$). (H) Micro-PET/CT imaging analysis of ^{68}Ga-DOTA-GSF/HSV in mouse brain with U87-MG cell xenograft. Micro-PET/CT imaging reconstruction was performed using PMOD software. (I) ^{68}Ga-DOTA-GSF/HSV biodistribution in the main organs was measured based on gamma counts ($n = 3$). (J) ^{68}Ga-DOTA-GSF/HSV biodistribution in the brain was measured based on gamma counts; $^{\#}p < 0.001$ was calculated using ANOVA ($n = 3$).

indicated that the peptides enabled the ability of ^{68}Ga-DOTA to target glioma. These results indicated that the peptides enabled the targeted binding ability of ^{68}Ga-DOTA via glioma uptake and allowed to visualize the glioma. GSF targeting showed better glioma targeting efficiency and displayed more visible and more gamma counts for glioma.

3.5. *Targeting liposome characterization*

The mean particle size of Lipo@Dox-Cy5.5, HSV-Lipo@Dox-Cy5.5, and GSF-Lipo@Dox-Cy5.5 was 32.37 ± 2.09 nm, 24.82 ± 2.51 nm, and 29.36 ± 3.84 nm, respectively (Fig. 5A). The PDI was 0.2 ± 0.01, 0.16

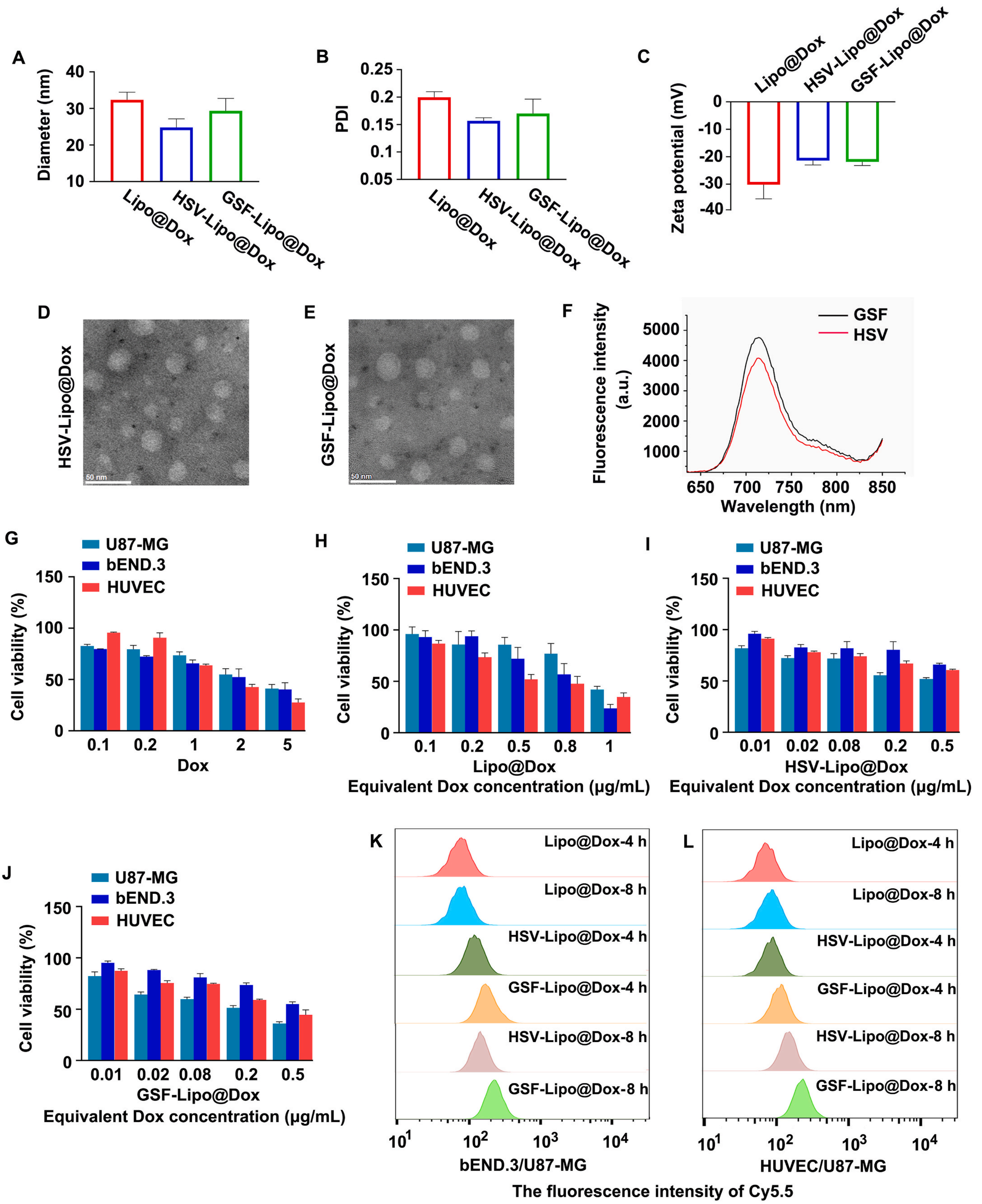

Fig. 5. Targeting liposome characterization. (A) Mean particle size of targeting liposome-Dox. (B) PDI of targeting liposome-Dox. (C) Zeta potential of targeting liposome-Dox. (D, E) Morphology of targeting liposome-Dox was observed using TEM. (F) Fluorescence intensity of liposome-Dox based on ultraviolet absorption. (G–J) Effects of Dox, Lipo@Dox, and targeting liposome-Dox on U87-MG cells, bEND.3 cells, and HUVECs. (K, L) Immunofluorescence analysis of Cy5.5 for targeting liposome-Dox uptake in U87-MG cells co-cultivated with bEND.3 cells and HUVECs.

± 0.01, and 0.17 ± 0.03, respectively (Fig. 5B). The zeta potential of the three liposomes with Cy5.5 modification was −30.19 ± 5.18 mV, −21.41 ± 1.81 mV, and −21.85 ± 1.39 mV, respectively (Fig. 5C). The morphology of GSF-Lipo@Dox and HSV-Lipo@Dox was observed using TEM and revealed that the desired nanoparticles had a spherical structure with a smooth surface (Fig. 5D and E). The encapsulation efficiency with Cy5.5 modification was 70 %, 85 %, and 78 %, respectively. The Dox-loading rate with Cy5.5 modification was 5.8 %, 7.3 %, and 6.2 %, respectively. The ultraviolet absorption spectrum is shown in Fig. 5F.

3.6. Cytotoxicity assay for Lipo@Dox

In vitro cytotoxicity of free Dox and Dox-loaded liposomes with different formulations was evaluated using bEND.3 cells, HUVECs, and U87-MG cells with a CCK-8 assay. Free Dox (Fig. 5G), Lipo@Dox (Fig. 5H), and peptide-Lipo@Dox (Fig. 5I and J) showed dose-dependent inhibition for U87-MG cell viability. After incubation with U87-MG cells for 24 h, the IC_{50} values (equivalent Dox concentration) for Dox, Lipo@Dox, HSV-Lipo@Dox, and GSF-Lipo@Dox were calculated based on the cytotoxicity results to be 3.49, 0.96, 0.55, and 0.26 μg/mL, respectively. Free Dox and Lipo@Dox showed high cytotoxicity in vascular endothelial cells, but peptide-Lipo@Dox showed lower cytotoxicity in bEND.3 cells compared to that in U87-MG cells and HUVECs. The highest cytotoxicity was observed in U87-MG cells with the same Dox concentration compared to the Dox and Lipo@Dox groups. The IC_{50} value for GSF-Lipo@Dox was lower than that for HSV-Lipo@Dox, indicating that GSF targeting was stronger than HSV-Lipo@Dox, while GSF-Lipo@Dox inhibition was greater than that of Lipo@Dox due to peptide targeting. These results showed that HSV-Lipo@Dox and GSF-Lipo@Dox targeting can decrease the effect of Dox concentration on glioma cells and reduce Dox cytotoxicity in normal cells.

3.7. ^{68}Ga-labeled targeting liposome-Dox use for glioma imaging

Next, bEND.3 cells or HUVECs and U87-MG cells were co-cultivated in the Transwells to simulate the BBB and BBTB. The targeting liposome-Dox penetration and binding abilities were then analyzed (Fig. 6A). Free Dox and Lipo@Dox formulations at a concentration of 1 μg/μL (equivalent Dox concentration, which is close to the IC_{50} value of Lipo@Dox) were added to the upper chamber and incubated for 4 and 8 h. Immunofluorescence results showed that U87-MG cell fluorescence intensity increased over time in the peptide-Lipo@Dox groups (Fig. 6A–C). Flow cytometry analysis indicated that the peptide-modified liposomes penetrated the vascular endothelial cells and were taken up by glioma

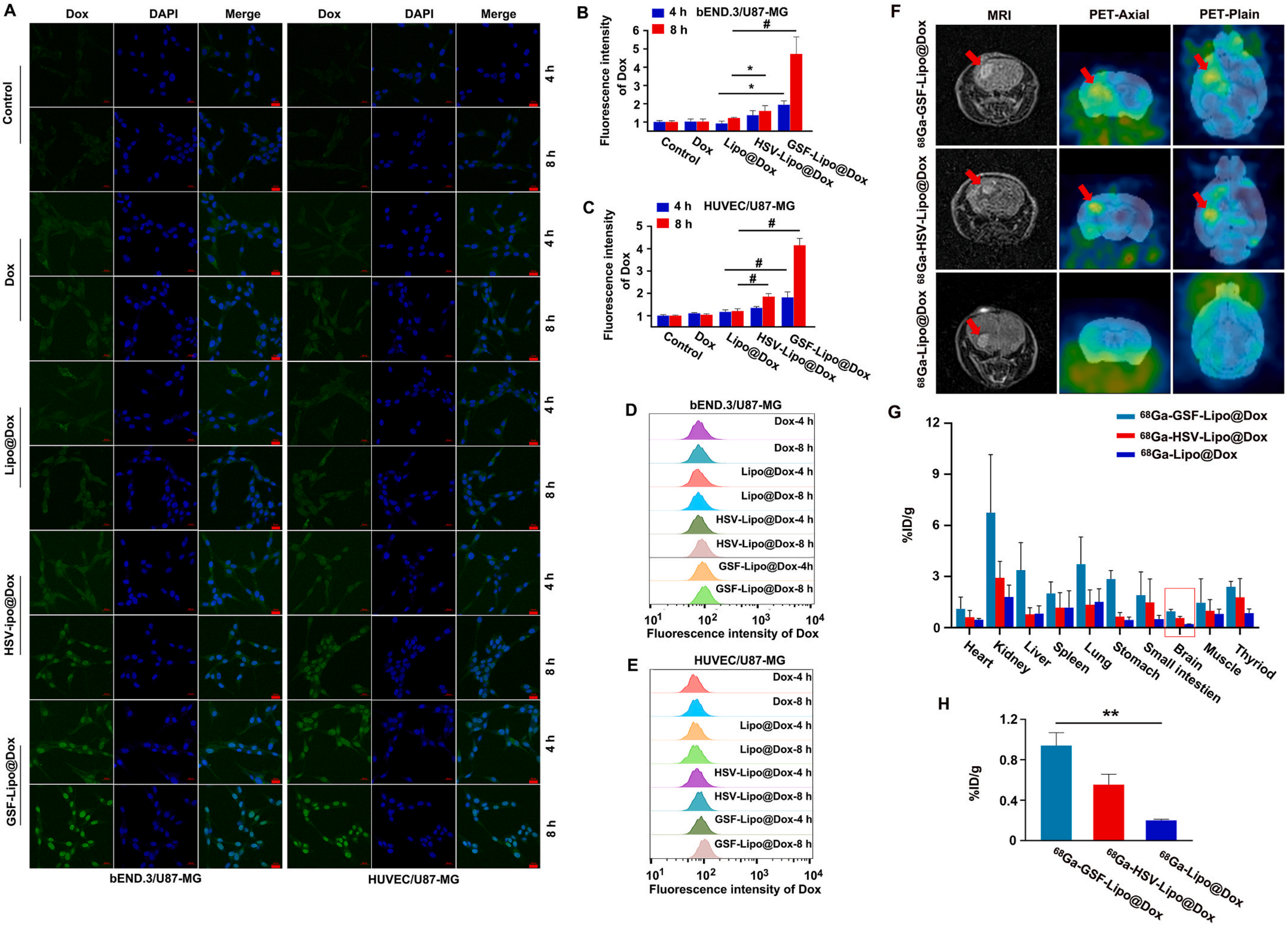

Fig. 6. Targeting liposome-Dox uptake and glioma imaging. (A) Immunofluorescence analysis of Dox uptake in U87-MG cells co-cultivated with bEND.3 cells and HUVECs; DAPI staining shows nucleoli (magnification, 400 × , bar = 50 μm). (B, C) Mean fluorescence intensity was measured using image J; $^{*}p < 0.05$, $^{\#}p < 0.001$ ($n = 6$). (D, E) Dox fluorescence intensity flow cytometry results for U87-MG cells co-cultivated with bEnd.3 cells and HUVECs. (F) Micro-PET/CT imaging analysis of ^{68}Ga-DOTA-GSF/HSV-Lipo@Dox in mouse brain with U87-MG cell xenograft and micro-PET/CT imaging reconstruction were performed using PMOD software. (G) ^{68}Ga-DOTA-GSF/HSV-Lipo@Dox biodistribution in main organs was measured based on gamma counts ($n = 2$). (H) ^{68}Ga-DOTA-GSF/HSV-Lipo@Dox biodistribution in the brain was measured based on gamma counts, $^{**}p < 0.01$ ($n = 2$).

cells (Fig. 6D and E). Moreover, GSF-Lipo@Dox fluorescence intensity was strongest among the three Dox-loaded liposomes (Fig. 6B–E), demonstrating that GSF/HSV-Lipo@Dox had a higher penetration efficiency than Lipo@Dox and enhanced cellular uptake of the formulations due to peptide targeting.

To investigate the use of ^{68}Ga-labeled DOTA-GSF/HSV-Lipo@Dox for glioma imaging, micro-PET/CT was used to detect the location of the orthotopic U87-MG cell tumor transplantation. Micro-PET/CT imaging (Fig. 6F) showed that the orthotopically transplanted U87-MG cell tumor could be visualized in the brain 30 min after ^{68}Ga-DOTA-GSF/HSV-Lipo@Dox injection compared to the ^{68}Ga-DOTA-Lipo@Dox results. The brain gamma counts in the ^{68}Ga-DOTA-GSF/HSV-Lipo@Dox groups were greater than those in the ^{68}Ga-DOTA-Lipo@Dox group (Fig. 6G and H). Thus, Dox-loaded nanoliposomes modified with ANGPT2 peptides could be used for glioma imaging. GSF targeting showed better glioma targeting efficiency and displayed more visible gamma counts for glioma.

3.8. Targeting liposome-Dox inhibited U87-MG cells via Tie-2/Akt/Foxo-1 pathway

It was determined that peptide-Lipo@Dox induced more apoptotic U87-MG cells than Lipo@Dox, especially in the GSF-Lipo@Dox group, with a significant difference in the apoptotic ratio compared to

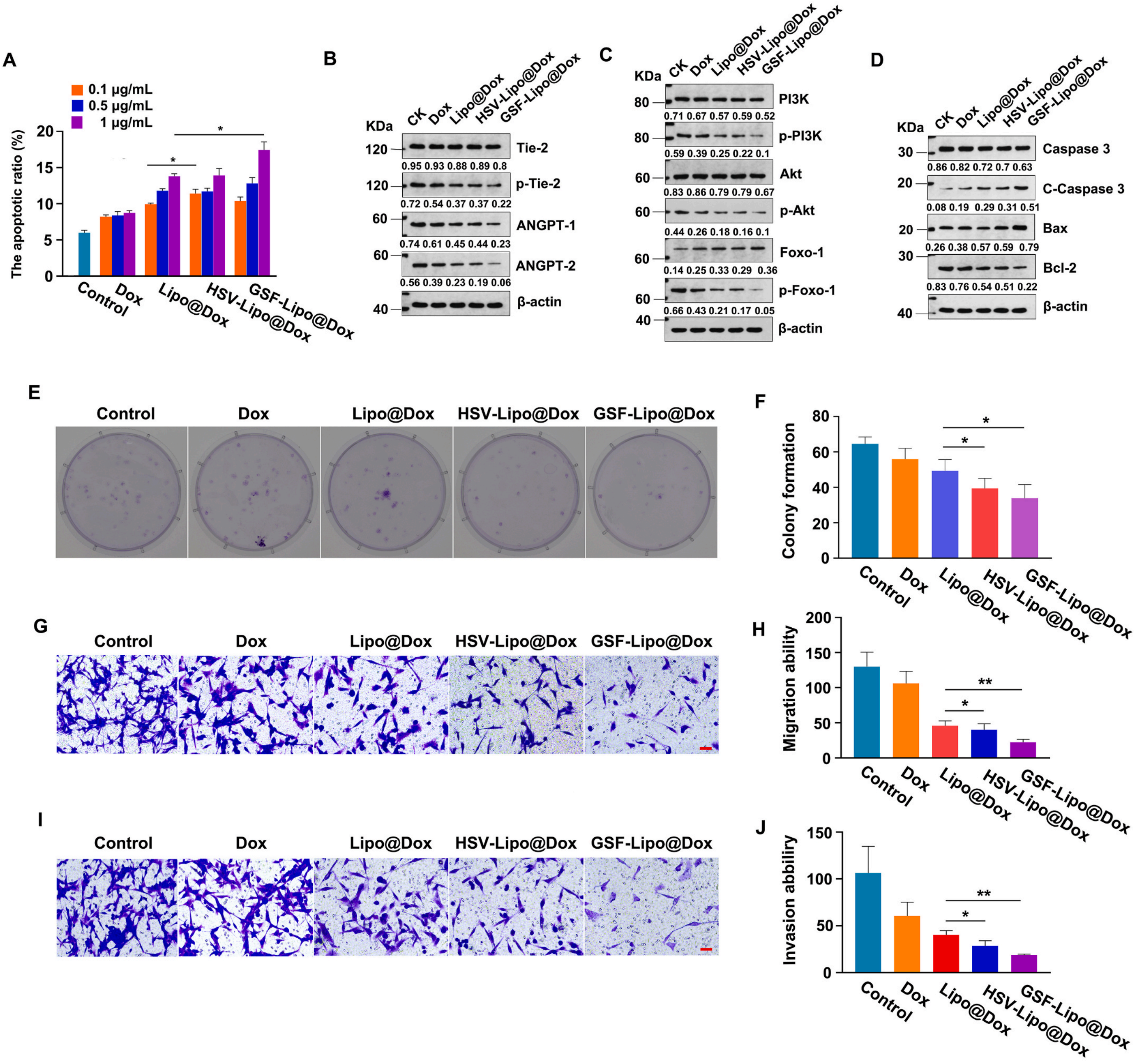

Fig. 7. Targeting liposome-Dox inhibited U87-MG cells via Tie-2/Akt/Foxo-1 pathway. (A) Apoptotic ratio for U87-MG cells treated with liposome-Dox for 24 h, *$p < 0.05$ ($n = 3$). (B–D) Protein levels were detected using IB and protein expression was quantified (target protein/β-actin). (E, F) Colony formation was observed and calculated; *$p < 0.05$ ($n = 3$). (G–J) U87-MG cells were seeded into Transwell chambers and treated with 1 μg/mL of Dox (effective liposome-Dox concentration) for 24 h. (G) Cell migration in the lower chamber was observed (magnification, 200 × , bar = 50 μm) and (H) the number of cells was quantified; *$p < 0.05$, **$p < 0.01$ ($n = 3$). (I) Cell invasion in the lower chamber was observed (magnification, 200 × , bar = 50 μm) and (J) the number of cells was determined; *$p < 0.05$, **$p < 0.01$ ($n = 3$).

Lipo@Dox at a concentration of 1 μg/μL (equivalent Dox concentration) (Fig. 7A). Representative flow cytometry images are shown in Fig. S10. Free Dox and Lipo@Dox formulations at a concentration of 1 μg/μL (equivalent Dox concentration) decreased the phosphorylation levels of Tie-2, Akt, PI3K, and Foxo-1 and decreased the expression levels of ANGPT1 and ANGPT2 (Fig. 7B and C). Free Dox and Lipo@Dox formulations also decreased the expression of Bcl-2 and increased the levels of cleaved caspase-3 and Bax (Fig. 7D). Protein expression decreased and increased more in the HSV-Lipo@Dox and GSF-Lipo@Dox groups due to peptide targeting.

In addition, free Dox and Lipo@Dox formulations inhibited colony formation (Fig. 7E and F) and decreased migration (Fig. 7G and H) and invasion counts (Fig. 7I and J) in U87-MG cells. HSV-Lipo@Dox and GSF-Lipo@Dox inhibition was greater than that of Lipo@Dox due to

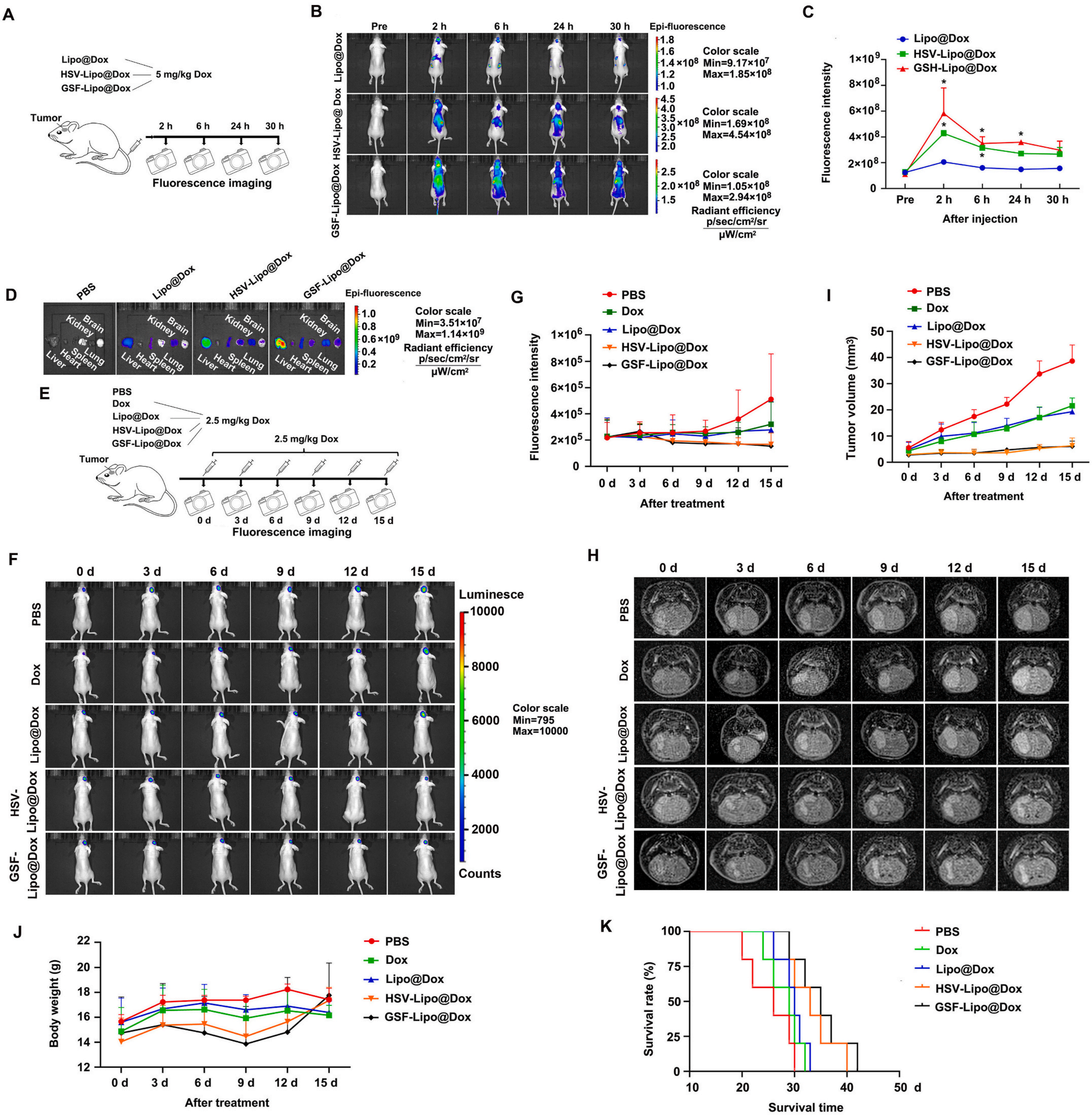

Fig. 8. *In vivo* anti-glioma effect of targeting liposome-Dox. (A) Liposome-Dox (5 mg/kg of effective Dox concentration) delivered via intracranial injection into orthotropic U87-MG cell glioma model mice and observed at different time points. (B) Distribution of Cy5.5-labeled targeting liposome-Dox at different time points in mice. (C) Fluorescence intensity observed in the head at different time points. (D) Fluorescence of brain and organs 30 h after injection. (E) Liposome-Dox (2.5 mg/kg of effective Dox concentration) delivered via intracranial injection into orthotropic U87-MG cell xenograft model and observed at different time points. (F) BLI of orthotopic U87-MG-luc cell xenograft model at different time points. (G) Fluorescence intensity of orthotopic U87-MG-luc cell xenograft, $n = 5$. (H) MRI of orthotopic U87-MG-luc cell xenograft at different time points in mice. (I) Comparation for volume of orthotopic U87-MG-luc cell xenograft at different time points in mice, $n = 5$. (J) Body weight of tumor-bearing mice at different time points, $n = 5$. (K) Survival rate after treatment.

peptide targeting. The above results suggested that peptide modification of liposomes enhanced the inhibitory effect of chemotherapeutic drugs on U87-MG glioma cells. In addition, targeting Lipo@Dox inhibited U87-MG cells via the ANGPT2/Tie-2/Akt/Foxo-1 pathway, and GSF had a stronger targeting effect than HSV. Therefore, GSF-Lipo@Dox inhibition was the most effective among the three Dox-loaded liposome groups.

3.9. Lipo@Dox targeting in orthotopic glioma model and organ distribution

Because of the short half-life of ^{68}Ga (approximately 60 min), peptide targeting could not be monitored for long periods of time *in vivo*. *In vivo* fluorescence imaging was performed to visualize the distribution of Lipo@Dox formulations in an orthotopic U87-MG cell tumor transplantation model. Lipo@Dox formulations were monitored 0, 2, 6, 24, and 30 h after tail vein injection (Fig. 8A). HSV-Lipo@Dox and GSF-Lipo@Dox were enriched in the brain for a longer time period than Lipo@Dox (Fig. 8B and C). Moreover, the GSF-Lipo@Dox fluorescence signal in the brain was stronger than that of HSV-Lipo@Dox after 30 h (Fig. 8D). HSV-Lipo@Dox and GSF-Lipo@Dox were abundantly distributed in organ angiogenesis, including in the liver, spleen, and lung, because ANGPT2 is a useful angiogenesis biomarker [32,33]. Therefore, these results suggested that the retention time of Lipo@Dox

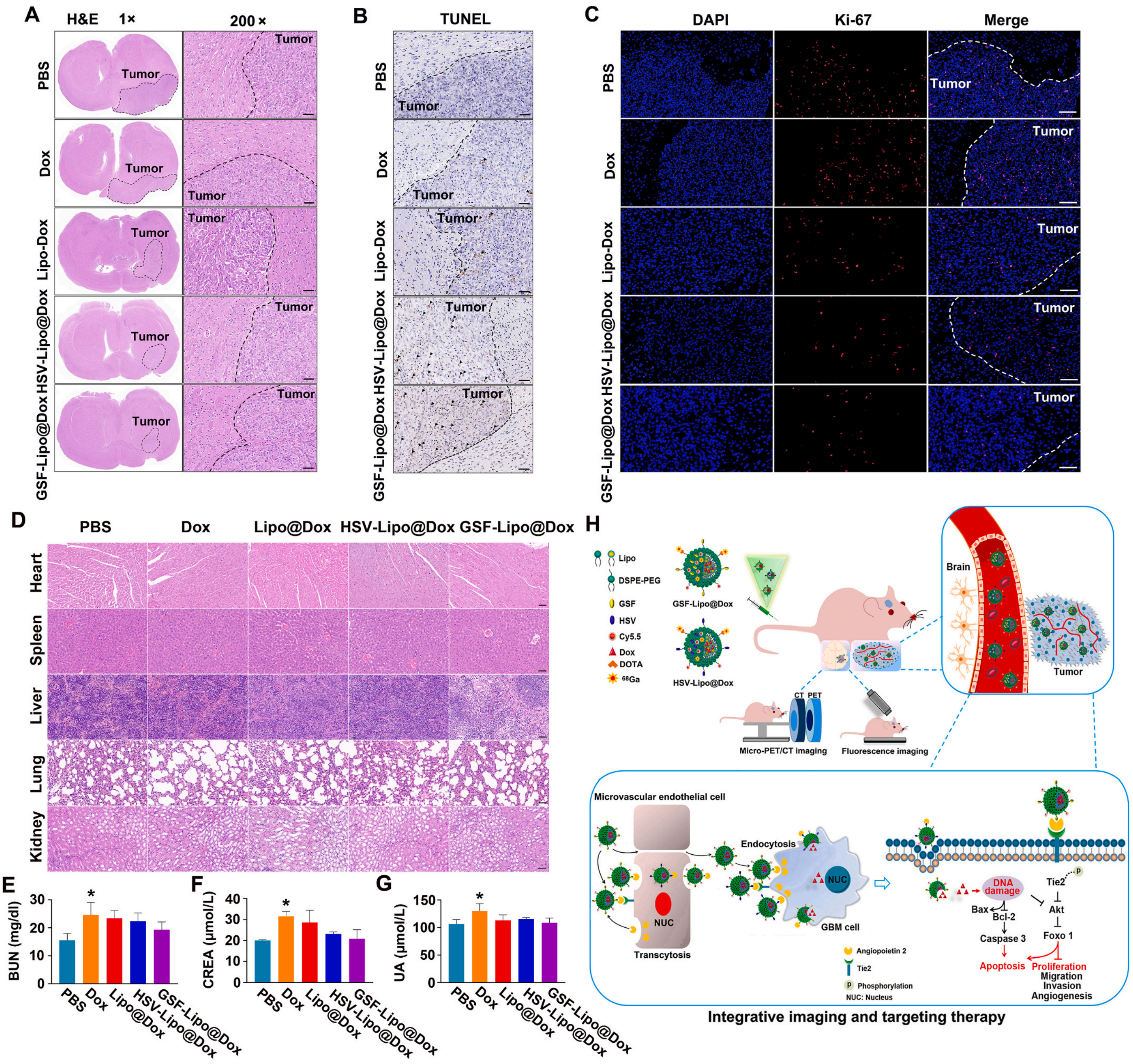

Fig. 9. Histological observation results for anti-tumor effect of targeting liposome-Dox. (A) H&E staining of orthotopic glioma. (B) TUNEL detection of apoptotic tumor cells; black arrows represent apoptotic tumor cells. (C) Immunofluorescence results for Ki-67 expression. (D) H&E staining analysis of toxicological effect of targeting liposome-Dox in different organs. (E) The BUN levels in plasma of orthotopic U87-MG-luc cell xenograft model after treatment, $*p < 0.05$ ($n = 3$). (F) The CREA levels in plasma of orthotopic U87-MG-luc cell xenograft model after treatment, $*p < 0.05$ ($n = 3$). (G) The UA levels in plasma of orthotopic U87-MG-luc cell xenograft model after treatment, $*p < 0.05$ ($n = 3$). (H) Target peptide-modified Lipo@Dox treatment inhibited U87-MG cell survival by inhibiting the Akt/GSK3β/β-catenin pathway. Lipo@Dox target peptide modification showed better suppression of glioma development than Lipo@Dox.

in the brain was prolonged due to the targeted effect of peptide modification.

3.10. *In vivo anti-glioma effect*

The changes in intracranial bioluminescence intensity of glioma were monitored in real time using BLI in an *in vivo* fluorescence imaging system (Fig. 8E and F). The bioluminescence intensities of the HSV-Lipo@Dox and GSF-Lipo@Dox groups were significantly weaker and smaller, respectively, than those of the other groups on day 6 (Fig. 8G). The glioma volume results monitored using an MRI system were consistent with those of BLI (Fig. 8H and I). Thus, HSV-Lipo@Dox and GSF-Lipo@Dox slowed down tumor growth (Fig. 8I). The body weight of mice was recorded to evaluate drug safety. Mouse body weight in the PBS, Dox, and Lipo@Dox groups was decreased on day 12. However, the body weight in the HSV-Lipo@Dox and GSF-Lipo@Dox groups increased starting on day 9 (Fig. 8J). Moreover, the HSV-Lipo@Dox and GSF-Lipo@Dox extended the survival time of tumor-bearing mice to 40 and 42 days after treatment, respectively (Fig. 8K).

After 15 days of treatment, H&E results showed that the Lipo@Dox formulations inhibited intracranial tumor growth, which was consistent with BLI and MRI results (Fig. 9A). The TUNEL assay results are shown in Fig. 9B. More apoptotic cells were detected using the TUNEL assay in the HSV-Lipo@Dox and GSF-Lipo@Dox groups than in the Lipo@Dox group (Fig. 9B), indicating that peptide-modified Lipo@Dox can enrich the orthotropic glioma tissue and plays a role in killing glioma cells. The fluorescence signal of Ki-67 in the HSV-Lipo@Dox and GSF-Lipo@Dox groups was weaker than that in the Lipo@Dox group (Fig. 9C), showing that Dox-loaded liposomes with peptide modification had a targeted inhibitory effect on glioma cells. The highest number of apoptotic cells and the weakest fluorescence signal of Ki-67 in the GSF-Lipo@Dox groups were noted due to the highest targeting ability. Thus, GSF-Lipo@Dox had a stronger killing and inhibitory effect on glioma cells than HSV-Lipo@Dox and exhibited the best anti-glioma activity among all groups. The pathological H&E staining images of main organ tissues after treatment are shown in Fig. 9D. There was no significant congestion, necrosis, or inflammation in the hearts, livers, spleens, kidneys, and lungs in the peptide-modified Lipo@Dox groups. The blood biochemical value results (BUN, CREA and UA levels) exhibited no significant differences between the control and peptide-modified Lipo@Dox groups and were within the normal range (Fig. 9E–G). The H&E staining and biochemical blood test results suggested that peptide-modified Lipo@Dox had no significant side effects in nude mice.

4. Dissusion

ANGPT2 expression is upregulated in a variety of human tumors, including neuroendocrine tumors [34], hepatocellular carcinoma, and gastric cancer [35]. ANGPT2 levels are elevated in patients with stage III and IV melanoma and colorectal cancer, which have a poor prognosis [36]. ANGPT2 up-regulation is associated with invasiveness displayed by human gliomas. Moreover, matrix metalloproteinase-2 and membrane type 1 matrix metalloproteinase induction by ANGPT2 may be essential for glioma invasion [37]. The present study found that the high ANGPT2 expression in glioma tissues was positively related to the stage and progression of glioma based on the TCGA dataset and immunohistochemistry analyses, further showing that ANGPT2 may be considered a glioma biomarker and has application potential in therapeutic targeting of glioma.

The role of ANGPT2 in angiogenesis is often thought of as an ANGPT1 antagonist that inhibits ANGPT1-promoted Tie-2 signaling, which is critical for vascular maturation and stability. ANGPT2 promotes Tie-2 phosphorylation by binding with it and then phosphorylates PI3K, leading to Akt phosphorylation [38]. Foxo-1 is activated by Akt phosphorylation, which significantly increases ANGPT2 mRNA level and promotes tumor cell survival and angiogenesis [11]. Therefore, we demonstrated for the first time that ANGPT2 activates the Tie-2/Akt/Foxo-1 signaling pathway and promotes the proliferation, invasion, and migration of glioma cells.

Our results showed high ANGPT2 expression in multiple glioma cells compared to glial cells. ANGPT2 knockdown caused G1 phase arrest, decreased cell viability, and increased apoptosis in U87-MG cells. Moreover, ANGPT2 silencing decreased cell proliferation and migratory and invasive capacities of U87-MG cells. However, increased ANGPT2 expression promoted cell proliferation, migration, and invasion of U87-MG cells. Angiogenesis-related ANGPT2/Tie2-system activated the PI3K/Akt pathway and phosphorylated Foxo-1, leading to an increase in ANGPT2 transcription and further promoting angiogenesis [39]. ANGPT2 knockdown decreased the endogenic binding of ANGPT2 and Tie-2 and phosphorylation levels of Akt and Foxo-1. On the contrary, increased ANGPT2 expression promoted the endogenic binding of ANGPT2 and Tie-2 and increased the phosphorylation levels of Akt and Foxo-1. In addition, ANGPT2 knockdown resulted in a decrease in Bcl-2 levels and an increase in apoptotic protein Bax and cleaved caspase-3 levels. This was consistent with previous study results, where ANGPT2 silencing resulted in a decrease in Bcl-2 levels and an increase in Bax levels in an oral squamous cell carcinoma model [40]. The above results suggested that ANGPT2 promoted glioma cell survival via the Tie-2/Akt/Foxo-1 pathway and provided new insights into the molecular function of ANGPT2 in regulatory mechanisms of glioma cells. The above results suggested that ANGPT2 contributes to oncogenic activity and can be an important biomarker for diagnosis and therapy of glioma.

Although ANGPT2 has been identified as a potential biomarker for glioma, it has been unclear how to use it to achieve precise targeted diagnosis and therapy. The BBB can weaken the efficiency of antibody drug conjugates entering the brain [41]. Thus, it was necessary to identify ANGPT2-specific ligands that easily penetrate the BBB, have low toxicity and high safety properties, and play a therapeutic role in glioma. Peptides are a good choice for use as ligands because of their small molecular weight, low immunogenicity *in vivo*, and high penetrability [42]. In the present study, a new sequence of peptides with eight amino acids and specific interaction with ANGPT2 was designed based on the crystal structure of ANGPT2. The uptake assay showed that the two peptides targeted both brain endothelial cells and tumor cells. Moreover, peptide-modified Dox-loaded liposomes effectively traversed the BBB and BBTB. The GSF uptake fluorescence intensity in the brain was higher than that of HSV modification and free Dox because the GSF targeting ability was stronger.

The poor permeability and limited distribution of Dox in solid tumors mean that it cannot be used as a chemotherapeutic agent [43]. Long-term circulating nanoparticles can deliver anti-cancer drugs to brain tumors by passively enhancing permeability and retention effects [44]. Moreover, liposomes are a potent carrier system for unique radionuclide-ligand complex delivery [45]. Thus, liposomes are a classic drug and radionuclide delivery carrier that is non-toxic and non-immunogenic. PEG modification on the surface of liposomes can prolong blood circulation duration to reach their therapeutic targets [46]. In the present study, liposomes with smaller particle sizes were designed and target peptides were modified on the surface of these liposomes. Longer circulation in the blood may provide more opportunities for stable GSF/HSV-modified liposomes to bind to ANGPT2.

Gallium-68 (^{68}Ga) is a positron-emitting isotope that is often attached to a specific chelating agent to be used as a tracer [47]. PEGylated liposomes were selected as delivery carriers for ^{68}Ga and Dox because liposomal Dox is a pioneering drug delivery system in a clinical setting (e.g. Doxil/Caelyx®) [48]. Simultaneous radionuclide and Dox delivery can help to explore the integrated theranostic potential of liposomal Dox in a clinical setting. The DSPE-PEG2000-GSF/HSV needs to be synthesized first to create peptide-modified liposomes. The synthetic design steps were based on a previous study [49]. The targeting copolymer DSPE-PEG2000-GSF/HSV was synthesized via nucleophilic substitution reaction between NHS and peptide N-terminal (Fig. S5).

Peptide and DSPE-PEG2000-NHS were dissolved in DMF and the pH of the mixture was adjusted to 8.2 using triethylamine. The reaction was carried out at room temperature for 12 h under moderate agitation. The conjugation was determined using H nuclear magnetic resonance spectroscopy (NMRS). The appearance of additional peptide peak is shown in Fig. S6, showing that it was not disturbed by DSPE-PEG2000-NHS. These results indicated that the peptides were successfully conjugated with DSPE-PEG2000. Bifunctional chelating, including EDTA, DOTA, and DOTPA binds the metal ($^{68}Ga^{3+}$ ion) to a complex with a high affinity for *in vivo* stability [50]. Thus, radiolabeling chelators have a significant impact on theranostics based on radiolabeling technology. The present study developed a Dox-loaded liposome formulation modified with Cy5.5 and DOTA peptides on the liposome surface. DOTA molecules were conjugated on the surface of the Dox-loaded liposome as a chelator for ^{68}Ga labeling. The DSPE-PEG2000 (or DSPE-PEG2000-GSF/HSV), DSPE-PEG2000-DOTA, DSPE-PEG2000-Cy5.5, and SPC were dissolved, evaporated, hydrated, extruded, encapsulated, and then dialyzed to prepare DOTA-conjugated Dox-loaded liposomes with peptide modification. Then, ^{68}Ga was attached to the DOTA chelator and the liposomal Dox was labeled to prepare the PEGylated liposome tracer. GSF/HSV-modified liposomes with ^{68}Ga labeling showed the location of glioma via micro-PET/CT imaging. Moreover, cell proliferation, migratory, and invasive abilities of U87-MG cells were significantly decreased in the GSF-Lipo@Dox and HSV-Lipo@Dox groups compared to those in the Lipo@Dox group. These results indicated that the targeted binding of GSF and HSV enabled cells to take up more Lipo@Dox, and the targeted binding effect of GSF was superior to that of HSV. Therefore, cell survival in the GSF-Lipo@Dox group was the lowest. In addition, Tie-2 expression and Akt and Foxo-1 phosphorylation levels decreased in the GSF-Lipo@Dox and HSV-Lipo@Dox groups, resulting in a decrease in Bcl-2 level and an increase in apoptotic protein Bax and cleaved caspase-3 levels. These results indicated that GSF/HSV-Lipo@Dox was targeted by peptides to inhibit cell survival via the ANGPT2/Tie-2/Akt/Foxo-1 pathway.

The uptake assay using Cy5.5 to label the two peptides showed that they targeted both endothelial and glioma cells, effectively traversing the BBTB. Their targeting ability with a longer circulation in intracranial glioma was further verified *in vivo* using fluorescence imaging. The GSF uptake fluorescence intensity was higher than that of HSV modification in the brain 30 h after administration, likely because the targeting ability of GSF was stronger. BLI and MRI were both used for *in vivo* monitoring of glioma growth in the present study because accurate monitoring of tumor volume after treatment is important to evaluate therapeutic effect of the drug. BLI is an indirect cell labeling technique employing reporter genes that converts chemical energy into visible light via the luciferase-catalyzed photon-emitting reaction in living animals [51]. BLI makes cell monitoring *in vivo* more convenient and cheaper and plays an important role in preclinical therapeutic efficacy monitoring of drugs in small animal models [52]. Even so, the loss and scatter of light *in vivo* limit the quantization accuracy, making the visualization of inner organs in the animal difficult and precluding clinical application [53]. Despite its weaknesses, BLI based on indirect labeling technique has been widely used to verify the therapeutic effect of nanoparticles on glioma due to the advantages of highest sensitivity [54]. In the present study, bioluminescence intensities of the peptide-modified Lipo@Dox groups were significantly weaker than those of the Lipo@Dox group 15 days after treatment due to the highest BLI sensitivity, which indicated that the glioma volume was smaller in the peptide-modified Lipo@Dox groups than in the Lipo@Dox group (Fig. 9). In order to verify the authenticity of glioma volume monitoring, MRI was used to observe the growth of intracranial orthotopic glioma because this method remains the gold standard for the investigation of central nervous system tumors in clinical diagnosis [55]. The glioma volume was smaller in the peptide-modified Lipo@Dox groups than in the Lipo@Dox group under MRI monitoring, which was consistent with BLI results. Therefore, BLI is a reliable method for monitoring intracranial orthotopic glioma changes in a mouse model. It can also be combined with MRI to improve the accuracy of monitoring. In the present study, free Dox-treated mice showed a rapidly decreasing body weight staring on day six of treatment, indicating that high toxicity of Dox impacted the body's function. However, the body weight of glioma-bearing mice gradually increased after 9 days of treatment, which pointed to the low toxicity and excellent therapeutic effects of peptide-modified Lipo@Dox on glioma. CREA, BUN and UA levels are the most widely used parameters for evaluating renal function [56]. Increases in their blood biochemical levels indicate nephrotoxicity [57]. H&E staining did not reveal obvious damage in the hearts, livers, kidneys, spleens, and lungs in the peptide-modified Lipo@Dox groups after treatment. Moreover, biochemical blood test results for renal function were not affected, further confirming the low toxicity and safety of peptide-modified Lipo@Dox.

5. Conclusion

In summary, two novel peptides targeting ANGPT2 were successfully designed and Dox-loaded nanoliposomes modified with these two peptides were prepared. Peptide-Lipo@Dox with ^{68}Ga labeling was used for glioma imaging. It also impeded U87-MG cell survival by inhibiting the ANGPT2/Tie-2/Akt/Foxo-1 pathway and showed a better suppression of glioma development than Lipo@Dox (Fig.9H) Therefore, ANGPT2 has application potential in glioma diagnosis and therapy, while ANGPT2-specific peptide-modified Lipo@Dox served as part of a potent drug delivery method for integrative imaging and targeting therapy of glioma.

CRediT authorship contribution statement

Hongyan Li: Writing – review & editing, Writing – original draft, Visualization, Validation, Resources, Methodology, Investigation, Funding acquisition, Conceptualization. **Rong Gan:** Visualization, Validation, Software, Methodology, Investigation, Formal analysis, Data curation. **Jiadi Liu:** Visualization, Validation, Software, Methodology. **Duling Xu:** Visualization, Validation, Software. **Qiyue Zhang:** Validation, Software, Investigation. **Haidong Tian:** Visualization, Validation. **Huijun Guo:** Visualization, Validation. **Haijun Wang:** Visualization, Resources. **Zhimin Wang:** Resources. **Xianwu Zeng:** Visualization.

Declaration of competing interest

We declare that we have no conflict of interest. We declare that the content of the manuscript is original and that it has not been published or accepted for publication, either in whole or in part, in any form (other than as an abstract or other preliminary publication). We declare that no part of the manuscript is currently under consideration for publication elsewhere.

Acknowledgments

This research was partially funded by the Natural Science Foundation for Distinguished Young Scholars of Gansu Province (23JRRA1349), the Western Young Scholars Program of Chinese Academy of Science (E223221YXB), the Significant Science and Technology Project of Gansu Province (232DFA014), the Program of the Local Science and Technology Development for Gansu Province Guided by Central Government (YDZX20216200001201), the Talent Team Project of Longyuan Youth Innovation and Entrepreneurship of Gansu Province (2023LQTD29), the Longyuan Young Talent Program of Gansu Province (E439221SR0), the Young Scientists Joint Fund of the Lanzhou Branch of Chinese Academy of Sciences (E490221XZ0), the Research Program of Heavy Ion Science and Technology Key Laboratory of IMP (HIST2024CO01), the National Natural Science Foundation of China (11875061), the Guangdong Basic and Applied Basic Research Foundation (2021A1515010027), the Major Joint Funds of Gansu Province

(23JRRA1537), the Program of Key Research and Development Program of Gansu Province (23YFFA0047).

Supplementary Material

Supplementary file 1. ANGPT2 sequence by three different siRNAs.

Supplementary file 2. ANGPT2 knockdown efficiency by three different siRNAs using real-time PCR.

Fig. S1. HPLC and MS identification results for GSF.

Fig. S2. HPLC and MS identification results for HSV.

Fig. S3. HPLC and MS identification results for FITC-GSF.

Fig. S4. HPLC and MS identification results for FITC-HSV.

Fig. S5. Structure and synthesis routes for DSPE-PEG2000-GSF/HSV.

Fig. S6. DSPE-PEG2000-GSF/HSV structures were confirmed by H-NMRS.

Fig. S7. HPLC and MS identification results for DOTA-GSF.

Fig. S8. HPLC and MS identification results for DOTA- HSV.

Fig. S9. Representative flow cytometry images for apoptosis and cell cycle.

Fig. S10. Representative flow cytometry images for apoptosis.

Appendix A. Supplementary data

Supplementary data to this article can be found online at https://doi.org/10.1016/j.mtbio.2025.101455.

Data availability

Data will be made available on request.

References

[1] J. Liu, A.M. Albrecht, X. Ni, J. Yang, M. Li, Glioblastoma tumor initiating cells: therapeutic strategies targeting apoptosis and microRNA pathways, Curr. Mol. Med. 13 (3) (2013) 352–357.

[2] B. Kasenda, D. König, M. Manni, R. Ritschard, U. Duthaler, E. Bartoszek, A. Bärenwaldt, S. Deuster, G. Hutter, D. Cordier, L. Mariani, J. Hench, S. Frank, S. Krähenbühl, A. Zippelius, C. Rochlitz, C. Mamot, A. Wicki, H. Läubli, Targeting immunoliposomes to EGFR-positive glioblastoma, ESMO Open 7 (1) (2022) 100365.

[3] S. Quader, K. Kataoka, H. Cabral, Nanomedicine for brain cancer, Adv. Drug Deliv. Rev. 182 (2022) 114115.

[4] J. Aparicio-Blanco, A.I. Torres-Suárez, Towards tailored management of malignant brain tumors with nanotheranostics, Acta Biomater. 73 (2018) 52–63.

[5] Y. Xia, C. Xu, X. Zhang, P. Ning, Z. Wang, J. Tian, X. Chen, Liposome-based probes for molecular imaging: from basic research to the bedside, Nanoscale 11 (2019) 5822–5838.

[6] N. Qi, S. Zhang, X. Zhou, W. Duan, D. Gao, J. Feng, A. Li, Combined integrin αvβ3 and lactoferrin receptor targeted docetaxel liposomes enhance the brain targeting effect and anti-glioma effect, J Nanobiotechnology 19 (2021) 446.

[7] M. Glas, H. Koch, B. Hirschmann, T. Jauch, A. Steinbrecher, U. Herrlinger, U. Bogdahn, P. Hau, Pegylated liposomal doxorubicin in recurrent malignant glioma: analysis of a case series, Oncology 72 (5–6) (2007) 302–307.

[8] S. Wagner, O. Peters, C. Fels, G. Janssen, A.K. Liebeskind, A. Sauerbrey, M. Suttorp, P. Hau, J.E. Wolff, Pegylated-liposomal doxorubicin and oral topotecan in eight children with relapsed high-grade malignant brain tumors, J. Neuro Oncol. 86 (2) (2008) 175–181.

[9] P. Chastagner, B. Devictor, B. Geoerger, I. Aerts, P. Leblond, D. Frappaz, J. C. Gentet, S. Bracard, N. André, Phase I study of non-pegylated liposomal doxorubicin in children with recurrent/refractory high-grade glioma, Cancer Chemother. Pharmacol. 76 (2) (2015) 425–432.

[10] W. Skiba, D. Suszczyk, A. Pawłowska, K. Włodarczyk, A. Pańczyszyn, I. Wertel, Clinical significance of tie-2-expressing monocytes/macrophages and angiopoietins in the progression of ovarian cancer-state-of-the-art, Cells 11 (23) (2022) 3851.

[11] R. Mazzieri, F. Pucci, D. Moi, E. Zonari, A. Ranghetti, A. Berti, L.S. Politi, B. Gentner, J.L. Brown, L. Naldini, M. De Palma, Targeting the ANG2/TIE2 axis inhibits tumor growth and metastasis by impairing angiogenesis and disabling rebounds of proangiogenic myeloid cells, Cancer Cell 19 (4) (2011) 512–526.

[12] A. Leong, M. Kim, The angiopoietin-2 and TIE pathway as a therapeutic target for enhancing antiangiogenic therapy and immunotherapy in patients with advanced cancer, Int. J. Mol. Sci. 21 (22) (2020) 8689.

[13] M. Chu, T. Li, B. Shen, X. Cao, H. Zhong, L. Zhang, F. Zhou, W. Ma, H. Jiang, P. Xie, Z. Liu, N. Dong, Y. Xu, Y. Zhao, G. Xu, P. Lu, J. Luo, Q. Wu, K. Alitalo, G.Y. Koh, R. H. Adams, Y. He, Angiopoietin receptor Tie2 is required for vein specification and maintenance via regulating COUP-TFII, Elife 5 (2016) e21032.

[14] M. Kim, B. Allen, E.A. Korhonen, M. Nitschké, H.W. Yang, P. Baluk, P. Saharinen, K. Alitalo, C. Daly, G. Thurston, D.M. McDonald, Opposing actions of angiopoietin-2 on Tie2 signaling and FOXO1 activation, J. Clin. Invest. 126 (9) (2016) 3511–3525.

[15] J. Bhachoo, T. Beuming, Investigating protein-peptide interactions using the schrödinger computational suite, Methods Mol. Biol. 1561 (2017) 235–254.

[16] S. Li, Z. Ding, X. Cao, Separation of Transglutaminase by Thermo-Responsive Affinity Precipitation Using L-Thyroxin as Ligand, vol. 5, Springer, 2016, p. 37.

[17] Y.C. Lo, W.J. Lin, Improve BBB penetration and cytotoxicity of palbociclib in U87-MG glioblastoma cells delivered by dual peptide functionalized nanoparticles, Pharmaceutics 15 (10) (2023) 2429.

[18] C. Chen, Z. Duan, Y. Yuan, R. Li, L. Pang, J. Liang, X. Xu, J. Wang, Peptide-22 and cyclic RGD functionalized liposomes for glioma targeting drug delivery overcoming BBB and BBTB, ACS Appl. Mater. Interfaces 9 (7) (2017) 5864–5873.

[19] C.M.G. da Silva, M. Franz-Montan, C.E.G. Limia, L.N.M. Ribeiro, M.A. Braga, V. A. Guilherme, C.B. da Silva, B.R. Casadei, C.M.S. Cereda, E. de, PaulaEncapsulation of ropivacaine in a combined (donor-acceptor, ionic-gradient) liposomal system promotes extended anesthesia time, PLoS One 12 (10) (2017) e0185828.

[20] G. Niu, B. Cogburn, J. Hughes, Preparation and characterization of doxorubicin liposomes, Methods Mol. Biol. 624 (2010) 211–219.

[21] D.N. Liu, M. Liu, S.S. Zhang, Y.F. Shang, F.H. Song, H.W. Zhang, G.H. Du, Y. H. Wang, Chrysomycin A inhibits the proliferation, migration and invasion of U251 and U87-MG glioblastoma cells to exert its anti-cancer effects, Molecules 27 (19) (2022) 6148.

[22] K.M. Sim, Y.S. Lee, H.J. Kim, C.H. Cho, G.S. Yi, M.J. Park, E.M. Hwang, J.Y. Park, Suppression of CaMKIIβ inhibits ANO1-mediated glioblastoma progression, Cells 9 (5) (2020) 1079.

[23] F.J. Núñez, F.M. Mendez, M.B. Garcia-Fabiani, J. Pardo, M. Edwards, P. R. Lowenstein, M.G. Castro, Evaluation of biomarkers in glioma by immunohistochemistry on paraffin-embedded 3D glioma neurosphere cultures, J. Vis. Exp. 143 (2019), https://doi.org/10.3791/58931.

[24] H. Li, Y. He, J. Yan, Q. Zhao, C. Di, H. Zhang, Comparative proteomics reveals the underlying toxicological mechanism of low sperm motility induced by iron ion radiation in mice, Reprod. Toxicol. 65 (2016) 148–158.

[25] H. Liu, C. Chen, J. Zeng, Z. Zhao, Q. Hu, MicroRNA-210-3p is transcriptionally upregulated by hypoxia induction and thus promoting EMT and chemoresistance in glioma cells, PLoS One 16 (7) (2021) e0253522.

[26] H. Li, L. Chen, J.J. Li, Q. Zhou, A. Huang, W.W. Liu, K. Wang, L. Gao, S.T. Qi, Y. T. Lu, miR-519a enhances chemosensitivity and promotes autophagy in glioblastoma by targeting STAT3/Bcl2 signaling pathway, J. Hematol. Oncol. 11 (1) (2018) 70.

[27] D.N. Liu, M. Liu, S.S. Zhang, Y.F. Shang, F.H. Song, H.W. Zhang, G.H. Du, Y. H. Wang, Chrysomycin A inhibits the proliferation, migration and invasion of U251 and U87-MG glioblastoma cells to exert its anti-cancer effects, Molecules 27 (19) (2022) 6148.

[28] L. Gherardini, V. Vetri Buratti, M. Maturi, G. Inzalaco, A. Locatelli, L. Sambri, S. Gargiulo, V. Barone, D. Bonente, E. Bertelli, S. Tortorella, L. Franci, A. Fioravanti, M. Comes Franchini, M. Chiariello, Loco-regional treatment with temozolomide-loaded thermogels prevents glioblastoma recurrences in orthotopic human xenograft models, Sci. Rep. 13 (1) (2023) 4630.

[29] M. Viale, V. Bertone, I. Maric, M. Cilli, L. Emionite, V. Bocchini, M. Ponzoni, V. Fontana, F. De Luca, M. Rocco, Enhanced therapeutic index of liposomal doxorubicin Myocet locally delivered by fibrin gels in immunodeficient mice bearing human neuroblastoma, Pharmacol. Res. 163 (2021) 105294.

[30] W. Lu, W. Liu, A. Hu, J. Shen, H. Yi, Z. Cheng, Combinatorial polydopamine-liposome nanoformulation as an effective anti-breast cancer therapy, Int J Nanomedicine 18 (2023) 861–879.

[31] A. Aloisio, N. Nisticò, S. Mimmi, D. Maisano, E. Vecchio, G. Fiume, E. Iaccino, I. Quinto, Phage-displayed peptides for targeting tyrosine kinase membrane receptors in cancer therapy, Viruses 13 (4) (2021) 649.

[32] Y. Osawa, S. Yoshio, Y. Aoki, M. Korenaga, M. Imamura, T. Oide, M. Okawara, H. Kawai, Y. Tsutsui, Y. Yoshida, S. Yoshikawa, T. Mori, T. Yamazoe, T. Kanto, Blood angiopoietin-2 predicts liver angiogenesis and fibrosis in hepatitis C patients, BMC Gastroenterol. 21 (1) (2021) 55.

[33] N. Enomoto, S. Suzuki, H. Hozumi, M. Karayama, Y. Suzuki, K. Furuhashi, T. Fujisawa, Y. Nakamura, K. Odagiri, T. Ishikawa, K. Kataoka, Y. Kondoh, M. Maekawa, N. Inui, H. Watanabe, T. Suda, Diagnostic and prognostic significance of serum angiopoietin-1 and -2 concentrations in patients with pulmonary hypertension, Sci. Rep. 11 (1) (2021) 15502.

[34] K.M. Detjen, S. Rieke, A. Deters, P. Schulz, A. Rexin, S. Vollmer, P. Hauff, B. Wiedenmann, M. Pavel, A. Scholz, Angiopoietin-2 promotes disease progression of neuroendocrine tumors, Clin. Cancer Res. 16 (2) (2010) 420–429.

[35] U.T. Hacker, L. Escalona-Espinosa, N. Consalvo, V. Goede, L. Schiffmann, S. J. Scherer, P. Hedge, E. Van Cutsem, O. Coutelle, H. Büning, Evaluation of Angiopoietin-2 as a biomarker in gastric cancer: results from the randomised phase III AVAGAST trial, Br. J. Cancer 114 (8) (2016) 855–862.

[36] M. Wieloch, M. Swiatkowska, M. Libiszewski, M. Hedayati, R. Drozda, K. Kołomecki, Assessment of the selected, late phase of angiogenesis factors' concentration in colorectal cancer patients, Pol Merkur Lekarski 27 (162) (2009) 466–469.

[37] P. Guo, Y. Imanishi, F.C. Cackowski, M.J. Jarzynka, H.Q. Tao, R. Nishikawa, T. Hirose, B. Hu, S.Y. Cheng, Up-regulation of angiopoietin-2, matrix metalloprotease-2, membrane type 1 metalloprotease, and laminin 5 gamma 2 correlates with the invasiveness of human glioma, Am. J. Pathol. 166 (3) (2005) 877–890.

[38] Z. Yang, W.H. Xia, Y.Y. Zhang, S.Y. Xu, X. Liu, X.Y. Zhang, B.B. Yu, Y.X. Qiu, J. Tao, Shear stress-induced activation of Tie2-dependent signaling pathway enhances reendothelialization capacity of early endothelial progenitor cells, J. Mol. Cell. Cardiol. 52 (5) (2012) 1155–1163.

[39] S. Chlench, N. Mecha Disassa, M. Hohberg, C. Hoffmann, T. Pohlkamp, G. Beyer, M. Bongrazio, L. Da Silva-Azevedo, O. Baum, A.R. Pries, A. Zakrzewicz, Regulation of Foxo-1 and the angiopoietin-2/Tie2 system by shear stress, FEBS Lett. 581 (4) (2007) 673–680.

[40] C. Li, Q. Li, Y. Cai, Y. He, X. Lan, W. Wang, J. Liu, S. Wang, G. Zhu, J. Fan, Y. Zhou, R. Sun, Overexpression of angiopoietin 2 promotes the formation of oral squamous cell carcinoma by increasing epithelial-mesenchymal transition-induced angiogenesis, Cancer Gene Ther. 23 (9) (2016) 295–302.

[41] B.M. Marin, K.A. Porath, S. Jain, M. Kim, J.E. Conage-Pough, J.H. Oh, C.L. Miller, S. Talele, G.J. Kitange, S. Tian, D.M. Burgenske, A.C. Mladek, S.K. Gupta, P. A. Decker, M.H. McMinn, S.A. Stopka, M.S. Regan, J.N. Sarkaria, Heterogeneous delivery across the blood-brain barrier limits the efficacy of an EGFR-targeting antibody drug conjugate in glioblastoma, Neuro Oncol. 23 (12) (2021) 2042–2053.

[42] X. Pan, J. Xu, X. Jia, Research progress evaluating the function and mechanism of anti-tumor peptides, Cancer Manag. Res. 12 (2020) 97–409.

[43] D. Wang, N. Zhang, T. Yang, Y. Zhang, X. Jing, Y. Zhou, J. Long, L. Meng, Amino acids and doxorubicin as building blocks for metal ion-driven self-assembly of biodegradable polyprodrugs for tumor theranostics, Acta Biomater. 147 (2022) 245–257.

[44] T.K. Shaw, P. Paul, Recent approaches and success of liposome-based nano drug carriers for the treatment of brain tumor, Curr. Drug Deliv. 19 (8) (2022) 815–829.

[45] I.O. Umeda, Y. Koike, M. Ogata, E. Kaneko, S. Hamamichi, T. Uehara, K. Moribe, Y. Arano, T. Takahashi, H. Fujii, New liposome-radionuclide-chelate combination for tumor targeting and rapid healthy tissue clearance, J Control Release 361 (2023) 847–855.

[46] F. Raza, L. Evans, M. Motallebi, H. Zafar, M. Pereira-Silva, K. Saleem, D. Peixoto, A. Rahdar, E. Sharifi, F. Veiga, C. Hoskins, A.C. Paiva-Santos, Liposome-based diagnostic and therapeutic applications for pancreatic cancer, Acta Biomater. 157 (2023) 1–23.

[47] A. Mishra, A. Carrascal-Miniño, J. Kim, R.T.M. de Rosales, [68Ga]Ga-THP-tetrazine for bioorthogonal click radiolabelling: pretargeted PET imaging of liposomal nanomedicines, RSC Chem Biol 5 (7) (2024) 622–639.

[48] I.M.O. Viana, S. Roussel, J. Defrêne, E.M. Lima, F. Barabé, N. Bertrand, Innate and adaptive immune responses toward nanomedicines, Acta Pharm. Sin. B 11 (4) (2021) 852–870.

[49] W. Zhao, Y. Xiong, D. Zhangsun, S. Luo, DSPE-PEG modification of α-conotoxin TxID, Mar. Drugs 17 (6) (2019) 342.

[50] J.P. Sinnes, U. Bauder-Wüst, M. Schäfer, E.S. Moon, K. Kopka, F. Rösch, 68Ga, 44Sc and 177Lu-labeled AAZTA5-PSMA-617: synthesis, radiolabeling, stability and cell binding compared to DOTA-PSMA-617 analogues, EJNMMI Radiopharm Chem 5 (1) (2020) 28.

[51] J.E. Kim, S. Kalimuthu, B.C. Ahn, In vivo cell tracking with bioluminescence imaging, Nucl Med Mol Imaging 49 (1) (2015) 3–10.

[52] S. Kalimuthu, J.H. Jeong, J.M. Oh, B.C. Ahn, Drug discovery by molecular imaging and monitoring therapy response in lymphoma, Int. J. Mol. Sci. 18 (8) (2017) 1639.

[53] B.C. Ahn, Applications of molecular imaging in drug discovery and development process, Curr Pharm Biotechnol 12 (4) (2011) 459–468.

[54] P.E. de Almeida, J.R. van Rappard, J.C. Wu, In vivo bioluminescence for tracking cell fate and function, Am. J. Physiol. Heart Circ. Physiol. 301 (3) (2011) H663–H671.

[55] A. Nikaki, G. Angelidis, R. Efthimiadou, I. Tsougos, V. Valotassiou, K. Fountas, V. Prasopoulos, P. Georgoulias, 18F-fluorothymidine PET imaging in gliomas: an update, Ann. Nucl. Med. 31 (7) (2017) 495–505.

[56] C. Pan, X. Wang, Z. Fan, W. Mao, Y. Shi, Y. Wu, T. Liu, Z. Xu, H. Wang, H. Chen, Polystyrene microplastics facilitate renal fibrosis through accelerating tubular epithelial cell senescence, Food Chem. Toxicol. 191 (2024) 114888.

[57] M.A.K. Abdelhalim, H.A. Qaid, Y. Al-Mohy, M.S. Al-Ayed, Effects of quercetin and arginine on the nephrotoxicity and lipid peroxidation induced by gold nanoparticles in vivo, Int J Nanomedicine 13 (2018) 7765–7770.